Compensation between Wnt-driven tumorigenesis and cellular responses to ribosome biogenesis inhibition in the murine intestinal epithelium

Aurélien Raveux, Aline Stedman, Sabrina Coqueran, Sandrine Vandormael-Pournin, Nick Owens, Béatrice Romagnolo, Michel Cohen-Tannoudji

Compensation between Wnt-driven tumorigenesis and cellular responses to ribosome biogenesis inhibition in the murine intestinal epithelium

Aurélien Raveux[1, 2, †], Aline Stedman[1, 3, †], Sabrina Coqueran[1], Sandrine Vandormael-Pournin[1], Nick Owens[4], Béatrice Romagnolo[5, 6, 7] and Michel Cohen-Tannoudji[1 #]

[1] : Early Mammalian Development and Stem Cell Biology, Institut Pasteur, CNRS UMR 3738, 25 rue du Dr. Roux, F-75015, Paris, France.

[2] : Sorbonne Université, Collège Doctoral, F-75005 Paris, France

[3] : present adress : Sorbonne Université, CNRS UMR7622, Inserm U1156, Institut de Biologie Paris Seine - Laboratoire de Biologie du Développement, 9 Quai Saint Bernard, F-75005 Paris, France.

[4] : Epigenetics of Stem Cells, Department of Developmental and Stem Cell Biology, Institut Pasteur, CNRS UMR3738, 25 rue du Docteur Roux, F-75015 Paris, France

[5] : Inserm, U1016, Institut Cochin, Paris, France

[6] : CNRS, UMR8104, Paris, France

[7] : Université Paris Descartes, Sorbonne Paris Cité, France

[†] : These authors contributed equally to the work

[#] Corresponding author and lead contact: Michel Cohen-Tannoudji, Early Mammalian Development and Stem Cell Biology, Institut Pasteur, CNRS UMR 3738, 25 rue du Dr. Roux, F-75015, Paris, France; E-mail: m-cohen@pasteur.fr; Phone: 33 1 45 68 84 86; Fax: 33 1 45 68 86 34; website: https://research.pasteur.fr/en/team/group-michel-cohen-tannoudji/.

Running title: Ribosome biogenesis defects and tumor initiation

Keywords : Ribosome biogenesis; Wnt signaling; Colorectal cancer; p53.

Abstract

Ribosome biogenesis inhibition causes cell cycle arrest and apoptosis through the activation of tumor suppressor-dependent surveillance pathways. These responses are exacerbated in cancer cells, suggesting that targeting ribosome synthesis may be beneficial to patients. Here, we characterize the effect of the loss-of-function of *Notchless* (*Nle*), an essential actor of ribosome biogenesis, on the intestinal epithelium undergoing tumor initiation due to acute *Apc* loss-of-function. We show that ribosome biogenesis dysfunction strongly alleviates Wnt-driven tumor initiation by restoring cell cycle exit and differentiation in *Apc*-deficient progenitors. Conversely Wnt hyperactivation attenuates the cellular responses to surveillance pathways activation induced by ribosome biogenesis dysfunction, as proliferation was maintained at control-like levels in the stem cells and progenitors of double mutants. Thus, our data indicate that, while ribosome biogenesis inhibition efficiently reduces cancer cell proliferation in the intestinal epithelium, enhanced resistance of *Apc*-deficient stem and progenitor cells to ribosome biogenesis defects may be an important concern when using a therapeutic strategy targeting ribosome production for the treatment of Wnt-dependent tumorigenesis.

INTRODUCTION

Ribosome biogenesis inhibition has emerged as a promising therapeutic strategy against cancer. Indeed, in addition to targeting the production of the ribosomes required for the increased protein synthesis demand of cancer cells[1], RNA Pol I inhibition or deficiencies in ribosome biogenesis factors were shown to trigger the binding of a 5S rRNA/RPL11/RPL5 inhibitory complex to MDM2, thereby preventing p53 degradation[2-4]. In absence of functional p53 pathway, ribosome biogenesis dysfunction also triggers p53-independent mechanisms[5]. Taking advantage of specific RNA Pol I inhibitors, several *in vitro* and xenograft studies have shown that lymphoma [6], melanoma, osteosarcoma, breast, colon [7] and lung [8] cancer cells display a strong and specific sensitivity to ribosome biogenesis inhibition, that induces potent p53-dependent or independent stress responses, which are not observed in normal cells[6,7]. As a therapeutic strategy, targeting the translational apparatus of cancer cells has two major advantages. Firstly, it is non-genotoxic and therefore minimizes the risk of inducing novel mutations in the surrounding cells. Secondly, this approach displayed so far a clear differential effect between normal cells and the tested cancer cell lines, making it theoretically possible to establish a dosage that reduces deleterious side effects while still being efficient. However, the impact of ribosome biogenesis alterations on tissues undergoing tumorigenesis *in vivo* has insufficiently been assessed until now.

In humans, APC is mutated in the vast majority of colorectal cancers [9]. In the mouse, the acute inactivation of *Apc* in the epithelium of the small intestine results in constitutive activation of the Wnt/β-catenin pathway, leading to an abnormal expansion of the proliferative compartment at the expense of differentiated cells, reminiscent of early events of adenoma formation[10,11]. It has been shown that *Myc* deletion largely rescues the *Apc* loss-of-function phenotype through downstream shutdown of the Wnt pathway[12], suggesting that Wnt-driven tumor initiation is also *Myc*-driven. Interestingly, the aforementioned Pol I inhibitors were demonstrated to be particularly efficient on *Myc*-driven cancer cells[6,8]. Since c-MYC is a major ribosome biogenesis positive regulator[13], this raised the possibility that ribosome biogenesis inhibition could also attenuate the phenotype caused by *Apc* deficiency.

Notchless (*Nle*) encodes a WD40 repeats-containing protein highly conserved in eukaryotes[14-16] and involved in the late steps of maturation and subsequent export of the

60S particle[17-20]. In previous studies, we showed that the role of *Nle* in the maturation of the large ribosomal subunit is conserved in the mouse[21], and that *Nle* loss-of-function leads to p53 activation in the intestinal epithelium, resulting in rapid stem cell and progenitor exhaustion through cell cycle arrest, apoptosis and premature goblet cell differentiation[22]. This genetic model offers a unique opportunity to study the impact of ribosome biogenesis perturbations specifically in the intestinal epithelium under pathological conditions. Here, by combining *Nle* and *Apc* conditional loss-of-function, we show that defective ribosome biogenesis strongly attenuates Wnt hyperactivation-driven proliferative compartment expansion in the intestinal epithelium through restoration of cell cycle exit and differentiation. Conversely, we show that Wnt hyperactivation alleviates the *Nle* loss-of-function phenotype, as proliferation is maintained in double mutant crypts and in the stem cell compartment despite broad and persistent p53 stabilization.

MATERIAL AND METHODS

Mice.

All experiments were conducted at the Institut Pasteur according to the French and European regulations on care and protection of laboratory animals (EC Directive 86/609, French Law 2001-486 issued on June 6, 2001) and were approved by the Institut Pasteur ethics committee (n° 2016-0106 and 2017-0044).

The alleles used were as follows: *Nle*^{flox} [21], *Nle*^{null} [15], *Apc*^{flox} [10], Villin-CreERT2 [23]. All experimental animals were generated in a mixed C57BL/6Nx129/Sv genetic background. Mice at 5 to 10 weeks of age were injected intraperitoneally with 56mg/kg tamoxifen for three consecutive days. For proliferation assays, mice were injected with BrdU (100 mg/kg) 2h, 24h or 48h before sacrifice. Injection order was randomized between animals and genotype was only assessed after the experiments.

Genotyping was performed by PCR after tissue lysis in 50 mM Tris, pH 8.5, 100 mM NaCl, 0.5% Tween 20, and 100 mg/ml proteinase K at 56°C overnight, followed by a 10-min incubation at 96°C. PCR was performed using 1.0 unit of Taq DNA polymerase (MP biomedicals) under the following conditions: 95 °C for 30 s; 32 cycles at 95 °C for 30 s, 60 °C for 30 s, 72 °C for 60 s; 72 °C for 10 min. For *Nle*, PCR amplification with primers mNleQF3 (5'- ctgtactctttctcatccgaccac -3'), CondF (5'- agacttggggtctggactca -3'), and CondR2 (5'- ccctaactaagacaaccaaga -3') allowed us to discriminate *Nle*^{wt} (100 bp), *Nle*^{Flox} (200 bp), and *Nle*^{del} (500 bp) alleles. For *Apc*, PCR amplification with primers APCint13F (5'- ctgttctgcagtatgttatca -3'), APCext14R (5'- ctatgagtcaacacaggatta -3'), and APCext15R (5'- caatataatgagctctgggcc -3') allowed us to discriminate *APC*^{wt} (180 bp), *Apc*^{Flox} (230 bp), and *Apc*^{del} (160 bp) alleles. PCR products were separated by electrophoresis on 2% high-resolution (NuSieve 3:1 agarose) agarose gels.

Tissue extracts.

For paraffin sections, the intestinal tract was dissected, then flushed with ice-cold PBS to remove feces and perfused with ice-cold 4% paraformaldehyde (PFA). The small intestine was rolled up from the proximal to the distal end in concentric circles, fixed in 4% PFA at 4°C overnight and embedded in paraffin wax. For RT-qPCR on total epithelium, 5 cm of duodenum was harvested in 10mL EDTA (10mM in PBS, pH=8.0). After 30 min incubation on ice and 2x5 min vortex at maximum speed at 4°C, the muscle layer of the intestine was

manually removed and the epithelium was pelleted at 300 rcf, 4°C for 5 min, then resuspended in 1 mL Trizol (Invitrogen, Carlsbad, CA, USA). For crypts and villi isolation, 5–10 cm of jejunum were collected, opened longitudinally and processed as previously described [24].

Histology and immunostaining.

Histology and immunostaining were performed as described previously [25]. Specific antibody binding was detected using biotinylated secondary antibodies and Streptavidin/HRP complexes (Dako, Glostrup, Denmark). For β-catenin immunostaining, M.O.M. and ABC kits (Vector) were used. Bright field microscopy was performed using a Axio Scan.Z1 equipped with a 20x objective lens. The system was set to run in automated batch mode with automated focus and tissue finding. Primary and secondary antibodies used in this study are listed in Supplementary material Supplementary Table S1.

In situ hybridization.

For Fluorescent In Situ Hybridization (FISH), the hybridization step was performed as previously described. Conjugated FISH probes were purchased from Eurogentec: its1-Cy5: tagacacggaagagccggacgggaaaga; its2-Cy3: gcgattgatcgtcaaccgacgctc and validated in a previous study [21]. ISH for Olfm4 was carried out with the RNAscope 2.5 BROWN kit (Advanced Cell Diagnostics) according to the manufacturer's instructions (Olfm4 probe reference: 311831).

RT-qPCR.

RNA extraction was performed according to the Trizol-chloroform extraction protocol provided by Invitrogen. For epithelium, crypts and villi, the chloroform and ethanol steps were repeated twice. Reverse-transcription was performed using the Superscript II kit (Invitrogen) according to the manufacturers' instructions. Real-time PCR was carried on using custom-designed primers (Supplementary Table S2) and LightCycler 480 SYBR Green I Master mix (Roche Life Sciences) on a LightCycler 480 (Roche Life Sciences). Expression levels were normalized using TBP and Aldolase as reference genes.

Western blot.

Proteins were extracted in a buffer containing 10mM Tris-HCl pH 7.5, 5mM EDTA, 150mM NaCl, 30mM Sodium Pyrophosphate, 50mM Sodium Fluoride, 10% Glycerol, 1% NP40, supplemented with antiproteases (Roche Life Sciences) and 2.5U/µL Benzonase (Sigma-Aldrich). The extracts were incubated on ice for 30 min, then centrifuged 10 min at 10000 rcf, 4°C. The supernatant was recovered and its protein content was determined using a Bradford assay. Proteins were denatured in Laemmli buffer at 95 °C for 5 min before being loaded on a 12% polyacrylamide gel. After migration, proteins were transferred onto a nitrocellulose membrane (Biorad, Hercules, CA, USA) and incubated overnight at 4°C with the primary antibodies. Membranes were incubated with peroxidase-labeled secondary antibodies at RT for 80 min and rinsed in TBS-0.1% Tween. Signals were visualized using ECl 2 (Pierce Biotechnology, Rockford, IL, USA) and quantified on a Typhoon Instrument. Primary and secondary antibodies used in these experiments are listed in Supplementary Table S1.

Quantification of protein synthesis.

Mice were injected intraperitoneally with 2mg of puromycin in PBS, 10min before sacrifice. Intestines were rapidly harvested in ice-cold PBS containing emetine to block further puromycin incorporation during the procedure. Crypts were isolated as previously described [24] and counted before being lysed in protein extraction buffer. Puromycilated peptide chains were quantified on a western blot against puromycin by measuring the pixel intensity through the whole length of each lane using a Typhoon instrument.

Crypts culture.

Isolated crypts were cultured as previously described [45]. In brief, crypts were embedded in growth factor reduced matrigel (Corning LifeSciences, Tewksbury, MA, USA) with culture medium (Advanced DMEM/F12; Invitrogen) containing EGF (Peprotech, Rocky Hill, NJ, USA), R-spondin 1 (R&D Systems, Minneapolis, MN, USA), Noggin (Peprotech) and B27 (Invitrogen). For nutlin-3 treatment, 4- or 8-days old organoids derived from Control or APC^{cKO} crypts were incubated with culture medium containing DMSO (mock condition) or nutlin-3a (Sigma) at 1µM, 5µM and 10µM concentrations. After 2 days of treatment, the number of healthy organoids was scored manually. Images of representative organoids were acquired with a bright-field Leica MZ16 binocular (Leica, M165FC). Healthy

organoids were defined as budding structures with at least 3 buds and visible lumen for Control, and smooth spheres with visible lumen for APC^{cKO}. 2 mice per genotype and 2 to 3 technical replicates per condition were assessed. For immunofluorescence, organoids were fixed in 4% formaldehyde for 2 hours at RT, permeabilized with Blocking Buffer (5% fetal calf serum, 0.5% Triton X-100 in 1X PBS) and incubated with appropriate primary and secondary antibodies. Phalloidin (1/50; Thermofisher) and DAPI (1/1000; Sigma) were used to detect cell membranes and nuclei, respectively. Samples were washed 3 times in PBS before being imaged on the macroapotome Zeiss Axiozoomer and analyzed using the Zen software.

Statistical analysis. All experiments were performed with a sample size n≥4 (each sample is an individual mouse) so as to dampen the influence of outliers on means. No animal was excluded from the analysis. For mean comparisons, all bar graphs with pooled data show means ± S.E.M. Statistical analyses were performed using the parametric Student's t-test and the non-parametric Mann–Whitney Wilcoxon test to account for the possibility of non-normal distributions. $p<0.05$ was considered significant. Tests were always two-sided.

RNA sequencing. Crypts were harvested at day 1 and day 2 pi from 3 mice of each genotypes and total RNA was prepared using Trizol-chloroform extraction. PolyA-enriched library preparation and PE150 sequencing were performed by Novogene Co. Ltd. Approximately 20 million sequences were generated per sample and used for the analysis. The sequence data have been deposited in NCBI's Gene Expression Omnibus under accession number GSE144233.

Computational Methods

RNA-seq Data Processing and Differential Expression

Paired end RNA-seq reads were quantified against the mm9 transcriptome using Kallisto 0.43 [26] with default options. Rounded estimated counts were used as input to DESeq2 [27]. Genes with at least 10 normalized counts in all replicates of at least one condition were considered for differential expression analysis. For all differential expression tests DESeq2 was run without independent filtering and without any fold change shrinkage, genes with padj < 0.05 are considered differentially expressed. Samples at 24h and 48h

were processed separately and subjected to the same analysis. We performed Wald tests under the model ~Nle + Apc + Nle:Apc, where Nle is a factor indicating Nle^{cKO} and Apc is a factor indicating Apc^{cKO}. Roughly, for each gene, the fold changes in Nle^{cKO} samples (N) and in Apc^{cKO} samples (A) were calculated. The interaction term (D) indicates that, for a given gene, the fold change in Apc^{cKO};Nle^{cKO} samples differs from N*A. We tested the significance of the Nle, Apc and the interaction term.

K-means clustering of RNA-seq Data

Response patterns of genes were identified using k-means clustering (using the Clustering package in Julia 0.6 [28]) on normalised read counts. We clustered the mean expression per timepoint and condition, normalised to the maximum expression of each gene. We found k = 10 provided a balance, both generalising broad behaviours and identify specific double cKO results.

Gene/phenotype ontology enrichment analysis

Genes were annotated with gene ontology (GO) terms (transitively closed to include parent terms) from the MGI GO annotation (date : 26/01/2017). Enrichment tests were applied to gene lists resulting from differential expression analysis. In all cases, enrichment tests were performed using χ^2 tests for all terms with at least 5 genes in the gene list of interest against a background of annotations of all genes tested for differential expression. χ^2 test p-values were adjusted by the Benjamini-Hochberg method, those with padj < 0.05 where reported.

The different gene clusters from the model-based analysis were also analyzed using the MouseMine database. For each gene list, Mammalian Phenotype Ontology Enrichment terms were searched with Max p-value = 0.05 and Holm-Bonferroni correction. When significantly enriched terms were found, those relevant to our mutant phenotypes were selected, and the term with the lowest p-value for each category was indicated on figures 5E and S5. For every analysis, $p<0.05$ is considered significant.

RESULTS

Nle loss-of-function improves survival of *Apc*-deficient mice and limits expansion of the crypt compartment.

Control (Villin-CreERT2$^{tg/0}$; *Apc*$^{flox/+}$; *Nle*$^{flox/+}$), Apc^{cKO} (Villin-CreERT2$^{tg/0}$; *Apc*$^{flox/flox}$; *Nle*$^{flox/+}$) and Apc^{cKO}; Nle^{cKO} (Villin-CreERT2$^{tg/0}$; *Apc*$^{flox/flox}$; *Nle*$^{flox/null}$) mice were subjected to three daily intraperitoneal tamoxifen injections and analyzed at various time points post last tamoxifen injection (pi) (Figure 1A). Conversion of the *Apc*^{flox} and *Nle*^{flox} alleles into *Apc*^{del} and *Nle*^{del} alleles respectively, was monitored by genomic PCR on both loci. We found that recombination of the *Apc*^{flox} and *Nle*^{flox} alleles was efficient in the intestinal epithelium from Control, Apc^{cKO} and Apc^{cKO}; Nle^{cKO} mice (Figure 1B). Apc^{cKO} mice lost weight and died rapidly following tamoxifen injection. Weight loss was significantly reduced in double mutant mice (Figure 1C), and although persisting, their death was significantly delayed compared to the Apc^{cKO} (Figure 1D).

Consistent with previous reports[10,11], hematoxylin-eosin staining showed that *Apc* loss-of-function resulted in rapid expansion of the crypt compartment at the expense of the villus (Figure 1E), loss of typical enterocyte polarity and abnormal nuclear morphology (Figure S1A). *Nle* loss-of-function strongly dampened these histological alterations (Figure 1E), as the enlarged crypt compartment was not observed, and cell polarity was restored in the villus (Figure S1A). Other aspects of the *Apc* loss-of-function phenotype such as the ectopic paneth cells[10] and enterocyte hypertrophia were similarly observed in Apc^{cKO}; Nle^{cKO} (Figure S1A-C). Collectively, these data indicate that *Nle* loss-of-function restores crypt and villus architecture in the *Apc*-deficient epithelium but does not fully rescue the *Apc* loss-of-function clinical and histological phenotype.

Nle loss-of-function attenuates proliferative compartment expansion by restoring cell cycle exit and differentiation despite Wnt pathway hyperactivation.

To verify that Wnt hyperactivation was effective in Apc^{cKO}; Nle^{cKO} intestinal epithelia, we monitored nuclear β-catenin on small intestine sections. Accumulation of nuclear β-catenin was similarly observed in Apc^{cKO} and Apc^{cKO}; Nle^{cKO} intestines (Figure 2A). Moreover, upregulation of the Wnt targets *c-Myc* and *Axin2* was found in both Apc^{cKO} and Apc^{cKO}; Nle^{cKO} epithelia (Figure 2B), confirming that hyperactivation of the Wnt/β-catenin pathway consecutive to *Apc*-deficiency was not modified by *Nle* loss-of-function.

We then performed a 2hrs BrdU chase to visualize proliferation in the intestinal epithelium at day 2, 3 and 4 pi (Figure 2C and S2A). As previously reported[10,11], proliferation in Apc^{cKO} intestines abnormally extended beyond the histological crypt compartment. Strikingly, the proliferation pattern was restored in Apc^{cKO}; Nle^{cKO}, as BrdU positive cells restricted to the histological crypt like in Control intestines (Figure 2C). The proportion of BrdU-positive cells within the proliferative compartment was similar for all genotypes (Figure 2D), suggesting that the structure of the cell cycle is not dramatically perturbed in Apc^{cKO} and Apc^{cKO}; Nle^{cKO} compared to Control. We observed a linear growth of their proliferative compartment overtime (Figure S2B-C), primarily due to enlarged crypt growth in Apc^{cKO}, whereas in Apc^{cKO}; Nle^{cKO}, it was caused by histological crypt hyperplasia (Figure S2A). Taken together, these data suggest that *Nle* loss-of-function reduces the expansion of the proliferative compartment consecutive to *Apc* loss-of-function without affecting the proliferation rate of *Apc*-deficient intestinal progenitors.

We next tested whether such attenuation could be due to a restoration of cell cycle exit by comparing the position of BrdU-positive cells after short and long periods of chase at day 2 and 3 pi. After 48h of chase, while BrdU-positive cells had exited cell cycle and were found in the villus in Control, all Apc^{cKO} BrdU-positive cells remained in the proliferative compartment (Figure 3A and S3A), thereby contributing to its expansion. Of note, BrdU staining was fainter in Apc^{cKO} than in Control, suggesting that Apc^{cKO} progenitors underwent more cell divisions than Control cells. In Apc^{cKO}; Nle^{cKO} intestine, BrdU-positive cells reached the villus after 48h chase at day 3pi. However, at day 2pi, BrdU-positive cells were found in the crypt and at the boundary between the crypt and the villus (Figure S3A-B) suggesting that though restored, cell-cycle exit is delayed in Apc^{cKO}; Nle^{cKO}. *Nle*-deficiency induced a potent apoptotic response in normal intestinal progenitors[22]. Caspase 3 staining on intestinal sections showed a similar proportion of Caspase-3-positive cells in both Apc^{cKO} and Apc^{cKO}; Nle^{cKO} proliferative compartments (Figure 3B, E), indicating that apoptosis is unlikely to be an important driver for the reduction of the proliferative compartment in the Apc^{cKO}; Nle^{cKO}. Finally, to evaluate the differentiation status of Apc^{cKO} and Apc^{cKO}; Nle^{cKO} epithelia, we performed Mucin-2 and Chromogranin-A immunohistochemistry (Figure 3C-D) and Alcian Blue coloration (Figure S3C). Enteroendocrine and goblet cells were absent from the expanded proliferative compartment of the Apc^{cKO} as previously reported[10,11]. In contrast, both cell types were found in Apc^{cKO}; Nle^{cKO} villi and crypts. Consistently, *Muc2* and *ChromoA* mRNA

levels in Apc^{cKO}; Nle^{cKO} crypts were intermediate compared to Apc^{cKO} and Controls (Figure 3F). Collectively, our results indicate that *Nle* loss-of-function attenuates Wnt hyperactivation-driven expansion of the proliferation compartment by partially restoring the capacity of *Apc*-deficient progenitors to exit cell cycle and differentiate.

Nle loss-of-function leads to ribosome biogenesis defects and p53 stabilization in the _Apc_-deficient epithelium.

The immediate consequences of *Apc* loss-of-function on ribosome biogenesis and protein synthesis in intestinal epithelium have not been described so far. No difference in the levels of nucleolar rRNA intermediates of the small (its1) and the large (its2) ribosomal subunits was observed in Apc^{cKO} compared to Control crypts at day 2 pi (Figure 4A-B) indicating that rRNA synthesis was not affected in *Apc*-deficient progenitors. Performing FISH with its1 and its2 probes, we previously showed increased ribosome biogenesis in crypts compared to villi[22]. Consistent with the invasion of proliferative cells into the villus region, FISH staining of Apc^{cKO} showed high pre-rRNAs levels in a region corresponding to the expanded proliferative compartment (Figure 4C). These data indicate that ribosome production in *Apc*-deficient proliferative cells is similar to that of *Apc*-proficient intestinal progenitors.

Nle loss-of-function was shown to affect large ribosomal subunit biogenesis in crypt cells [22] leading to the specific increase in its2, but not its1, levels. A similar phenotype was detected in Apc^{cKO}; Nle^{cKO} crypts at day 2 pi (Figure 4B-C), however its2 accumulation was no longer restricted to crypt cells but largely extended to villi (Figure 4C). A possible explanation for this observation would be that Apc^{cKO}; Nle^{cKO} progenitors, unlike Nle^{cKO} (Villin-CreERT2$^{tg/0}$; *Nle*$^{flox/null}$) progenitors, survived and continued to proliferate despite dysfunctional ribosome biogenesis, thereby giving rise to differentiated cells with increased nucleolar ribosomal pre-particles.

We next asked whether these defects activated a p53 stress response, as in a normal epithelium[22]. In Apc^{cKO}, p53 was transiently stabilized at day 2 pi in a few cells located at the distalmost part of the expanded proliferative compartment (Figure 4D and S4A) consistent with previous reports[29]. In Apc^{cKO}; Nle^{cKO}, strong and persistent p53 nuclear staining was observed in most cells of the crypt and of the lower part of the villus (Figure 4D and S4B), like its2 accumulation (Figure 4C). Importantly, robust p53 stabilization was observed in Apc^{cKO}; Nle^{cKO} progenitors in absence of cell cycle arrest

(Figures 2A and S2) or massive apoptotic response (Figure 3B) contrary to Nle^{cKO} crypt cells[22]. Collectively, our data show that *Nle* loss-of-function leads to defective ribosome biogenesis and p53 stabilization in *Apc*-deficient progenitor cells without triggering the cell cycle arrest and apoptotic responses normally observed in *Apc*-proficient cells.

The double mutant transcriptome is essentially the sum of single mutant transcriptomes.

We performed RNAseq on Control, Nle^{cKO}, Apc^{cKO} and Apc^{cKO}; Nle^{cKO} crypts at day 1 and 2 pi (Figure 5; Supplementary Table S3). Principal component analysis clearly distinguished samples according to their genotype (Figure 5A), with PC1 (58.79% of the variance) and PC2 (12.77% of the variance) segregating the samples according to the *Apc* or *Nle* genotype respectively. Apc^{cKO}; Nle^{cKO} samples were undistinguishable from Apc^{cKO} according to PC1 and from Nle^{cKO} according to PC2, indicating that Apc^{cKO}; Nle^{cKO} is essentially the linear combination of Nle^{cKO} and Apc^{cKO}. Using K-means clustering, we found that the 15115 genes expressed in our dataset could be spread into 10 clusters with distinct gene expression variation patterns (Figure 5B; Supplementary Table S4). Strikingly, the vast majority of the genes had the same expression pattern in Apc^{cKO}; Nle^{cKO} as in Apc^{cKO}, with only four clusters (6, 7, 9 and 10) comprising 3259 (21%) genes that were differentially regulated in Apc^{cKO}; Nle^{cKO} compared to Apc^{cKO} samples. Gene expression pattern varied little according to the timing.

To distinguish additive from non-additive interactions between the two mutations, we performed a model-based analysis where timings were considered separately (Figure 5C-D). Considering all samples at a given time point, a "*Nle*-related", an "*Apc*-related" fold-change and an interaction term describing the deviation of the double mutant from a linear combination of the two mutants were calculated for each gene. Examining cases where the effects of the double mutant were either an independent combination of both, or exhibited a dependence, we distinguished 8 gene categories (Figure 5C; Supplementary Table S5), four of which encompassed genes that were subject to non-additive interactions (*ie* have a "D" term). Consistent with the principal component analysis, *Apc* loss-of-function was largely dominant compared to *Nle* loss-of-function (91% vs 38% of misregulated genes at day 2 pi) (Figure 5D). Besides genes that were either unaffected in all genotypes ([-|-|-]) and those affected only by *Apc* or *Nle* loss of function ([A|-|-] and [-|N|-]), a minority of genes was subject to either additive ([A|N|-], 15% of misregulated

genes at day 2 pi) or non-additive interactions ([-|-|D], [-|N|D], [A|-|D], and [A|N|D], 14% of misregulated genes at day 2 pi) (Figure 5D). Gene and phenotype ontology enrichment analysis (Figures 5E and S5) showed that *Apc* or *Nle* loss of function upregulated genes involved in ribosome biogenesis in an additive manner (Figure 5E, [A|N|-]). Interestingly, the sub-cluster of genes that are expressed at intermediate levels in Apc^{cKO}; Nle^{cKO} due to the additive effect of Apc-related upregulation and Nle-related downregulation is significantly enriched in genes involved in cell cycling and proliferation (Figure 5E, [A|N|-]). Overall, hypothesizing that the observed phenotypic differences arises from differential gene regulation at the transcriptional level, these results suggest that the phenotype of the Apc^{cKO}; Nle^{cKO} essentially results from additive gene-by-gene effects of *Apc* and *Nle* loss-of-function rather than signaling pathway transcriptional activation or shutdown.

We next examined a few sets of genes whose differential expression might be relevant to the Apc^{cKO}; Nle^{cKO} phenotype (Figure 5F). Upregulation of cell cycle inhibitor genes in Apc^{cKO}; Nle^{cKO} progenitors compared to Apc^{cKO} might explain their enhanced capacity to stop proliferating. However, *p21* was the only cell cycle inhibitor upregulated in Apc^{cKO}; Nle^{cKO} to levels similar to Nle^{cKO}. This was likely due to p53 activation since *p21* is a well-known p53 target. Other p53 targets were equally upregulated in Apc^{cKO}; Nle^{cKO} and Nle^{cKO}, including those that were downregulated in the Apc^{cKO} (*Fas*, *Perp*). Thus, Wnt hyperactivation does not dramatically impact *p53* transcriptional response. Conversely, most Wnt targets were similarly upregulated in Apc^{cKO}; Nle^{cKO} and Apc^{cKO}, suggesting that *Nle* loss-of-function only marginally modulates the Wnt hyperactivation transcriptional response. Finally, intestinal stem cell marker expression in Apc^{cKO}; Nle^{cKO} resulted from either additive (*Ascl2, Sox9, Tert, Pw1, Bmi1*) or non-additive (*Olfm4, Lgr5, Mex3a, Lrig1, Krt15, Hopx*) effects. Strikingly, *Nle* loss-of-function attenuated Wnt hyperactivation-driven *Lgr5* upregulation but also participated to the synergic upregulation of the reserve stem cell markers *Krt15* and, to a lesser extend *Hopx* and *Bmi1*. This suggests that the reserve intestinal stem cell population might be particularly stimulated in the Apc^{cKO}; Nle^{cKO} intestine.

Nle loss-of-function leads to a reduction of mature rRNAs and protein synthesis activity in _Apc_-deficient crypts.

We next asked whether alterations in ribosome content and protein synthesis activity could contribute to the phenotype. We first quantified the levels of mature rRNAs (18S and 28S) by RT-qPCR (Figure 4A). No difference in rRNA levels was observed in Apc^{cKO} crypts compared to Control at day 2 pi (Figure 6A) indicating that, like pre-rRNA, ribosome content was not affected in *Apc*-deficient progenitors. We also monitored protein synthesis by puromycin incorporation *in vivo*[22]. Surprisingly, quantification of puromycylated nascent chains after a short *in vivo* pulse of puromycin revealed an increased number of active ribosomes in *Apc*-deficient progenitors compared to the control at day 2 and day 3 pi (Figure 6B-C, S6). Taken together with the aforementioned analyses of pre-rRNA levels, these data indicate that upregulation of protein synthesis, but not ribosome biogenesis, is an early feature of Apc-deficient progenitors.

Interestingly, contrary to the Nle^{cKO}, mature rRNA levels were significantly decreased in Apc^{cKO}; Nle^{cKO} crypts (Figure 6A). It can be hypothesized that progenitor survival and proliferation despite ribosome biogenesis defects in the Apc^{cKO}; Nle^{cKO} gives rise to cells with decreased ribosome content. Strikingly, the number of active ribosomes in Apc^{cKO}; Nle^{cKO} crypt cells reduced to normal level compared to Apc^{cKO} (Figure 6B-C, S6). Altogether, these data suggest that, in the context of *Apc*-deficient intestinal epithelium, *Nle* loss-of-function leads to a reduction of ribosome content consecutive to ribosome biogenesis defects, which, in turn, decreases translational activity of *Apc*-deficient progenitors to control-like levels. Such impairment of translation stimulation might contribute to induce cell cycle exit in Apc^{cKO}; Nle^{cKO} progenitors.

Wnt hyperactivation prevents p53-induced rapid depletion of intestinal stem and progenitor cells in *Nle*-deficient crypts.

We then examined the fate of intestinal stem cells in Apc^{cKO}; Nle^{cKO} mice. RT-qPCR confirmed the transcriptomic data as *Lgr5* was upregulated in the Apc^{cKO} and restored to control levels in the Apc^{cKO}; Nle^{cKO} at day 2 pi, whereas *Olfm4* was downregulated in both Nle^{cKO} and Apc^{cKO}; Nle^{cKO} compared to Control (Figure 7A). *In situ* hybridization indicated that, as expected, *Olfm4* expression confined to cells at the crypt bottom in Control, extended upward in Apc^{cKO} and was markedly decreased in Nle^{cKO} (Figure 7B). In Apc^{cKO}; Nle^{cKO}, *Olfm4* staining was similar to Apc^{cKO} but varied from crypt to crypt and was generally fainter than both Control and Apc^{cKO}. Interestingly, nuclear p53 protein was detected in crypt base columnar (CBC) cells, recognizable by their shape and location at

the crypt base, at every tested time point (Figure 7C) suggesting that, like progenitors, *Apc*-deficient stem cells were less sensitive to ribosome biogenesis defects and p53 activation than *Apc*-proficient stem cells. Indeed, contrary to Nle^{cKO}, proliferating CBCs were present at the bottom of Apc^{cKO}; Nle^{cKO} crypts (Figure 7D). Collectively, these data show that intestinal stem and progenitor cells are maintained in Apc^{cKO}; Nle^{cKO} mice despite defective ribosome biogenesis and robust p53 activation.

To confirm this point, we derived organoids from control, Nle^{cKO}, Apc^{cKO} and Apc^{cKO}; Nle^{cKO} crypts harvested at day 1 pi (Figure 8A-B). Contrary to Nle^{cKO} crypts, Apc^{cKO}; Nle^{cKO} crypts grew into organoids at the same rate as Control (Figure 8A). Of note, Apc^{cKO}; Nle^{cKO} organoids grew as spheroids like Apc^{cKO} (Figure 8B). Over time, Apc^{cKO}; Nle^{cKO} organoids were progressively populated by *Nle*-proficient cells that had escaped recombination at the *Nle* locus. This, together with the fact that continuous Cre induction is detrimental to organoid growth [46], prevented us to assess the behavior of Apc^{cKO}; Nle^{cKO} organoids at later time points. In order to highlight possible increased resistance to p53 activation of Apc^{cKO} stem and progenitor cells compared to Control, we cultured organoids with increasing doses of nutlin-3, a small compound that activates p53 through inhibition of Mdm2. Apc^{cKO} organoids were more resistant to nutlin-3 treatment than Control, as viability of Control was strongly reduced at 5µM nutlin-3 while that of APC^{cKO} organoids was almost unaffected (Figure 8D) despite robust p53 stabilization (Figure S7B). Collectively, these results show that Apc^{cKO}; Nle^{cKO} intestinal stem and progenitor cells display enhanced survival to p53 activation.

DISCUSSION

Colorectal cancers, like many cancers, are characterized by increased ribosome biogenesis and protein translation[30,31]. High expression of pre-rRNA is associated with poor prognosis in colorectal cancer[32] and increased translational elongation is key for intestinal tumorigenesis[33]. Interestingly, oxaliplatin, a drug commonly used to treat colorectal cancers, was shown to affect ribosome biogenesis and trigger p53 induction and, consistent with this, cancer cells sensitive to oxaliplatin display higher ribosome biogenesis and mRNA translation rates[34]. Here, we showed that *in vivo* gut epithelium-specific inhibition of ribosome biogenesis strongly attenuates the expansion of the proliferative compartment during tumor initiation.

Inactivation of some key target genes of the Wnt/β-catenin pathway such as *c-Myc*[12], *cyclinD2*[35] and *Fak1*[36] or of the chromatin remodeling factor *Brg1*[37] were also shown to dampen the expansion of the proliferative compartment in Apc^{cKO} mice. In all these situations, dampening was accompanied by a marked alteration of the Wnt hyperactivation transcriptional signature. In contrast, *Nle* loss-of-function only marginally modifies the transcriptomic response to *Apc* loss-of-function. The partial rescue of Apc^{cKO}; Nle^{cKO} mice phenotype is thus rather due to the compensation between the antagonistic effects of Wnt-driven tumorigenesis and ribosome biogenesis inhibition.

In Apc^{cKO}; Nle^{cKO} mice, attenuation likely results from the activation of the RP/MDM2/p53 ribosome biogenesis surveillance pathway. Upon *Apc* inactivation, p53 stabilization is observed only locally and transiently in a small population of cells and the intestinal phenotype of *Apc* loss-of-function is not modified in absence of p53 (this study and [29]). In contrast, high levels of p53 are detected in Apc^{cKO}; Nle^{cKO} crypt and villus cells showing dysfunctional ribosome biogenesis, recognizable by their nucleolar accumulation of precursor rRNAs of the large ribosomal subunit. Contrary to *Apc*-deficient progenitors, Apc^{cKO}; Nle^{cKO} progenitors are able to exit cell cycle and differentiate. Upregulation by p53 of *p21* could be contributing to the restoration of cell cycle arrest and attenuation of the expansion of the proliferative compartment. Another explanation for this attenuation is that Apc^{cKO}; Nle^{cKO} progenitors are unable to upregulate protein synthesis at a level sufficient for tumorigenesis. We show here that increased protein translation is an immediate hallmark of *Apc* loss-of-function that is no longer observed in Apc^{cKO}; Nle^{cKO} progenitors. Enhanced translation likely increases the

production of important rate-limiting cell cycle regulators and could influence the capacity of cells to divide or not. Similar to *Nle* loss-of-function, genetic or pharmacologic inhibition of mTORC1-dependent translational stimulation limits the expansion of the proliferative compartment during tumor initiation[33]. The reduction of the translational potential of Apc^{cKO}; Nle^{cKO} progenitors may therefore contribute to their eventual cell cycle exit and differentiation.

Apc-deficiency dramatically modifies the cellular responses of intestinal cells to defective ribosome biogenesis. Indeed, while Apc^{cKO}; Nle^{cKO} stem cells and progenitors express high levels of nuclear p53 and display a clear p53 transcriptional signature, they do not elicit the strong proliferation arrest and apoptotic responses normally observed in crypt cells[22]. Crosstalk between the Wnt/β-catenin pathway and p53 have been previously reported and involve the direct or indirect modulation of p53 stability by GSK3[38,39]. However, the regulation of p53 activity by GSK3 leads to p53 degradation, suggesting that this is not the mechanism through which *Apc* loss-of-function attenuates p53 activation in Apc^{cKO}; Nle^{cKO} crypt cells. Rather, the fate of stem and progenitor cells with an activated RP/MDM2/p53 ribosome biogenesis surveillance pathway may be modified by the transcriptional response to Wnt/β-catenin hyperactivation, such as for example increased expression of *Ppan*, which has been previously shown to elicit anti-apoptotic activities in intestinal stem cells and progenitors[40]. On a different note, it has been shown that the Wnt pathway modulates protein stoichiometry of polysomal ribosomes during mouse neocortex development[41], which, in turns could potentially result in significant modulation of the proteome[42]. If it holds true in the intestine, such qualitative changes in translation may also contribute to the different behaviors of intestinal cells to p53 activation.

It is unclear why intestinal progenitors eventually exit cell cycle in Apc^{cKO}; Nle^{cKO} mice. Disequilibrium between the antagonistic actions of Wnt hyperactivation and defective ribosome biogenesis may trigger proliferation arrest. The extended proliferative compartment of the *Apc* mutant is in many respects heterogeneous, in particular regarding p53 stabilization (this study and [29]) and p21 expression[43], which concern a small population of cells located at the leading edge of the proliferative compartment. It is therefore possible that while leaving the crypt domain, Apc^{cKO}; Nle^{cKO} progenitors experience a suprainduction of p53 and p21, which, together with increased concentration of pro-differentiation cues such as BMPs, trigger cell cycle exit. At the same

time, Apc^{cKO}; Nle^{cKO} progenitors located in the crypt domain are able to proliferate despite defective ribosome biogenesis, giving rise to cells with reduced numbers of ribosomes. Such decrease may also be interpreted as a signal for proliferation arrest, as suggested by the impaired proliferation of primary human cell lines with a defective RP/MDM2/p53 ribosome biogenesis surveillance pathway[44].

Our work also unravels major modifications of the *Nle* loss-of-function phenotype by *Apc*-deficiency. Importantly, our demonstration that *Apc*-deficient stem cells and progenitors are resistant to defective ribosome biogenesis challenges the notion that cancer cells, and in particular c-MYC-driven cancer cells, are more sensitive to ribosome biogenesis inhibition than normal cells[6-8]. Moreover, enhanced survival of stem cells to ribosome biogenesis stress under Wnt hyperactivation conditions may be a major limitation for therapeutic strategies targeting ribosome production, not only for colorectal cancers, but also for other cancers associated with deregulation of the Wnt/β-catenin pathway such as cutaneous melanoma, breast carcinoma, hepatocarcinoma or pancreatic ductal adenocarcinoma.

AKNOWLEDGMENTS

Imaging analyses was performed at the Imagopole and the histopathology Unit of the Institut Pasteur. We are grateful to the staff of the animal facility of Institut Pasteur for animal care and their help during this work. We thank G. Comai for technical help and advices on RNAscope ISH.This work was supported by the Fondation ARC pour le Recherche sur le cancer (PGA120140200873), the Institut Pasteur, the Centre National de la Recherche Scientifique, the Agence Nationale de la Recherche (ANR-10-LABX-73-01 REVIVE) and the Institut National du Cancer (INCa 2007-1-COL-6-IC-1 and PLBIO09-070). A.R. was supported by the Université Pierre et Marie Curie and received fellowship from the French Ministère de l'Enseignement Supérieur et de la recherche, the Fondation ARC pour la Recherche sur le Cancer and the REVIVE Labex. A. S. received support from the Fondation des Treilles.

Competing interests : The authors declare no competing interest.

REFERENCES

1 Ruggero D, Pandolfi PP. Does the ribosome translate cancer? *Nat Rev Cancer* 2003; **3**: 179–192.

2 Fumagalli S, Ivanenkov VV, Teng T, Thomas G. Suprainduction of p53 by disruption of 40S and 60S ribosome biogenesis leads to the activation of a novel G2/M checkpoint. *Genes & Development* 2012; **26**: 1028–1040.

3 Bursać S, Brdovčak MC, Pfannkuchen M, Orsolić I, Golomb L, Zhu Y *et al.* Mutual protection of ribosomal proteins L5 and L11 from degradation is essential for p53 activation upon ribosomal biogenesis stress. *Proceedings of the National Academy of Sciences* 2012; **109**: 20467–20472.

4 Donati G, Peddigari S, Mercer CA, Thomas G. 5S ribosomal RNA is an essential component of a nascent ribosomal precursor complex that regulates the Hdm2-p53 checkpoint. *Cell Rep* 2013; **4**: 87–98.

5 Challagundla KB, Sun X-X, Zhang X, DeVine T, Zhang Q, Sears RC *et al.* Ribosomal protein L11 recruits miR-24/miRISC to repress c-Myc expression in response to ribosomal stress. *Mol Cell Biol* 2011; **31**: 4007–4021.

6 Bywater MJ, Poortinga G, Sanij E, Hein N, Peck A, Cullinane C *et al.* Inhibition of RNA Polymerase I as a Therapeutic Strategy to Promote Cancer-Specific Activation of p53. *Cancer Cell* 2012; **22**: 51–65.

7 Peltonen K, Colis L, Liu H, Trivedi R, Moubarek MS, Moore HM *et al.* A targeting modality for destruction of RNA polymerase I that possesses anticancer activity. *Cancer Cell* 2014; **25**: 77–90.

8 Kim DW, Wu N, Kim Y-C, Cheng P-F, Basom R, Kim D *et al.* Genetic requirement for Mycl and efficacy of RNA Pol I inhibition in mouse models of small cell lung cancer. *Genes & Development* 2016; **30**: 1289–1299.

9 Brannon AR, Vakiani E, Sylvester BE, Scott SN, McDermott G, Shah RH *et al.* Comparative sequencing analysis reveals high genomic concordance between matched primary and metastatic colorectal cancer lesions. *Genome Biol* 2014; **15**: 454.

10 Andreu P, Colnot S, Godard C, Gad S, Chafey P, Niwa-Kawakita M *et al.* Crypt-restricted proliferation and commitment to the Paneth cell lineage following Apc loss in the mouse intestine. *Development* 2005; **132**: 1443–1451.

11 Sansom OJ, Reed KR, Hayes AJ, Ireland H, Brinkmann H, Newton IP *et al.* Loss of Apc in vivo immediately perturbs Wnt signaling, differentiation, and migration. *Genes & Development* 2004; **18**: 1385–1390.

12 Sansom OJ, Meniel VS, Muncan V, Phesse TJ, Wilkins JA, Reed KR *et al.* Myc deletion rescues Apc deficiency in the small intestine. *Nature* 2007; **446**: 676–679.

13 van Riggelen J, Yetil A, Felsher DW. MYC as a regulator of ribosome biogenesis and protein synthesis. *Nat Rev Cancer* 2010; **10**: 301–309.

14 Royet J, Bouwmeester T, Cohen SM. Notchless encodes a novel WD40-repeat-containing protein that modulates Notch signaling activity. *Embo J* 1998; **17**: 7351–7360.

15 Cormier S, Le Bras S, Souilhol C, Vandormael-Pournin S, Durand B, Babinet C *et al.* The Murine Ortholog of Notchless, a Direct Regulator of the Notch Pathway in Drosophila melanogaster, Is Essential for Survival of Inner Cell Mass Cells. *Mol Cell Biol* 2006; **26**: 3541–3549.

16 Gazave E, Lapébie P, Richards GS, Brunet F, Ereskovsky AV, Degnan BM *et al.* Origin and evolution of the Notch signalling pathway: an overview from eukaryotic genomes. *BMC Evol Biol* 2009; **9**: 249.

17 la Cruz de J, Sanz-Martínez E, Remacha M. The essential WD-repeat protein Rsa4p is required for rRNA processing and intra-nuclear transport of 60S ribosomal subunits. *Nucleic Acids Research* 2005; **33**: 5728–5739.

18 Ulbrich C, Diepholz M, Baßler J, Kressler D, Pertschy B, Galani K *et al.* Mechanochemical Removal of Ribosome Biogenesis Factors from Nascent 60S Ribosomal Subunits. *Cell* 2009; **138**: 911–922.

19 Matsuo Y, Granneman S, Thoms M, Manikas R-G, Tollervey D, Hurt E. Coupled GTPase and remodelling ATPase activities form a checkpoint for ribosome export. *Nature* 2014; **505**: 112–116.

20 Barrio-Garcia C, Thoms M, Flemming D, Kater L, Berninghausen O, Baßler J *et al.* Architecture of the Rix1-Rea1 checkpoint machinery during pre-60S-ribosome remodeling. *Nat Struct Mol Biol* 2015; **23**: 37–44.

21 Le Bouteiller M, Souilhol C, Cormier S, Stedman A, Burlen-Defranoux O, Vandormael-Pournin S *et al.* Notchless-dependent ribosome synthesis is required for the maintenance of adult hematopoietic stem cells. *Journal of Experimental Medicine* 2013; **210**: 2351–2369.

22 Stedman A, Beck-Cormier S, Le Bouteiller M, Raveux A, Vandormael-Pournin S, Coqueran S *et al.* Ribosome biogenesis dysfunction leads to p53-mediated apoptosis and goblet cell differentiation of mouse intestinal stem/progenitor cells. *Cell Death Differ* 2015; **22**: 1865–1876.

23 Marjou El F, Janssen K-P, Chang BH-J, Li M, Hindie V, Chan L *et al.* Tissue-specific and inducible Cre-mediated recombination in the gut epithelium. *Genesis* 2004; **39**: 186–193.

24 Guo J, Longshore S, Nair R, Warner BW. Retinoblastoma protein (pRb), but not p107 or p130, is required for maintenance of enterocyte quiescence and differentiation in small intestine. *J Biol Chem* 2009; **284**: 134–140.

25 Léguillier T, Vandormael-Pournin S, Artus J, Houlard M, Picard C, Bernex F *et al.* Omcg1 is critically required for mitosis in rapidly dividing mouse intestinal progenitors and embryonic stem cells. *Biol Open* 2012; **1**: 648–657.

26 Bray NL, Pimentel H, Melsted P, Pachter L. Near-optimal probabilistic RNA-seq quantification. *Nat Biotechnol* 2016; **34**: 525–527.

27 Love MI, Huber W, Anders S. Moderated estimation of fold change and dispersion for RNA-seq data with DESeq2. *Genome Biol* 2014; **15**: 550.

28 Bezanson J, Edelman A, Karpinski S, Shah VB. Julia: A Fresh Approach to Numerical Computing. *SIAM Review* 2017; **59**: 65–98.

29 Reed KR, Meniel VS, Marsh V, Cole A, Sansom OJ, Clarke AR. A limited role for p53 in modulating the immediate phenotype of Apc loss in the intestine. *BMC Cancer* 2008; **8**: 162.

30 Pelletier J, Thomas G, Volarevic S. Ribosome biogenesis in cancer: new players and therapeutic avenues. *Nat Rev Cancer* 2017; **4**: a003681.

31 Bastide A, David A. The ribosome, (slow) beating heart of cancer (stem) cell. *Oncogenesis* 2018; **7**: 34.

32 Tsoi H, Lam KC, Dong Y, Zhang X, Lee CK, Zhang J *et al.* Pre-45s rRNA promotes colon cancer and is associated with poor survival of CRC patients. *Oncogene* 2017. doi:10.1038/onc.2017.86.

33 Faller WJ, Jackson TJ, Knight JRP, Ridgway RA, Jamieson T, Karim SA *et al.* mTORC1-mediated translational elongation limits intestinal tumour initiation and growth. *Nature* 2015; **517**: 497–500.

34 Bruno PM, Liu Y, Park GY, Murai J, Koch CE, Eisen TJ *et al.* A subset of platinum-containing chemotherapeutic agents kills cells by inducing ribosome biogenesis stress. *Nature Medicine* 2017; **23**: 461–471.

35 Cole AM, Myant KB, Reed KR, Ridgway RA, Athineos D, van den Brink GR *et al.* Cyclin D2–Cyclin-Dependent Kinase 4/6 Is Required for Efficient Proliferation and Tumorigenesis following Apc Loss. *Cancer Research* 2010; **70**: 8149–8158.

36 Ashton GH, Morton JP, Myant KB, Phesse TJ, Ridgway RA, Marsh V *et al.* Focal adhesion kinase is required for intestinal regeneration and tumorigenesis downstream of Wnt/c-Myc signaling. *Dev Cell* 2010; **19**: 259–269.

37 Holik AZ, Young M, Krzystyniak J, Williams GT, Metzger D, Shorning BY *et al.* Brg1 loss attenuates aberrant wnt-signalling and prevents wnt-dependent tumourigenesis in the murine small intestine. *PLoS Genet* 2014; **10**: e1004453.

38 Eom T-Y, Jope RS. GSK3 beta N-terminus binding to p53 promotes its acetylation. *Mol Cancer* 2009; **8**: 14.

676 39 Kulikov R, Boehme KA, Blattner C. Glycogen synthase kinase 3-dependent
677 phosphorylation of Mdm2 regulates p53 abundance. *Mol Cell Biol* 2005; **25**: 7170–
678 7180.

679 40 Pfister AS, Keil M, Kühl M. The Wnt Target Protein Peter Pan Defines a Novel p53-
680 independent Nucleolar Stress-Response Pathway. *Journal of Biological Chemistry*
681 2015; **290**: 10905–10918.

682 41 Kraushar ML, Viljetic B, Wijeratne HRS, Thompson K, Jiao X, Pike JW *et al.* Thalamic
683 WNT3 Secretion Spatiotemporally Regulates the Neocortical Ribosome Signature
684 and mRNA Translation to Specify Neocortical Cell Subtypes. *Journal of Neuroscience*
685 2015; **35**: 10911–10926.

686 42 Genuth NR, Barna M. Heterogeneity and specialized functions of translation
687 machinery: from genes to organisms. *Nat Rev Genet* 2018; **13**: 1.

688 43 Cole AM, Ridgway RA, Derkits SE, Parry L, Barker N, Clevers H *et al.* p21 loss blocks
689 senescence following Apc loss and provokes tumourigenesis in the renal but not the
690 intestinal epithelium. *EMBO Mol Med* 2010; **2**: 472–486.

691 44 Teng T, Mercer CA, Hexley P, Thomas G, Fumagalli S. Loss of tumor suppressor
692 RPL5/RPL11 does not induce cell cycle arrest but impedes proliferation due to
693 reduced ribosome content and translation capacity. *Mol Cell Biol* 2013; **33**: 4660–
694 4671.

695 45 Sato T, Vries RG, Snippert HJ, van de Wetering M, Barker N, Stange DE *et al.* Single
696 Lgr5 stem cells build crypt-villus structures in vitro without a mesenchymal niche.
697 *Nature* 2009; **459**: 262–265.

698 46 Bohin N, Carlson EA, Samuelson LC. Genome Toxicity and Impaired Stem Cell
699 Function after Conditional Activation of CreERT2 in the Intestine. *Stem Cell Reports*
700 2018; **11**: 1337–1346.

701

FIGURE LEGENDS

Figure 1 *Nle* loss-of-function improves survival of *Apc*-deficient mice and limits crypt hyperplasia. (A) Scheme of tamoxifen injection and analysis. (B) Detection of the nonrecombined (flox) and the recombined (del) *Apc* (top) and *Nle* (bottom) alleles by PCR performed on DNA extracts from Control, Apc^{cKO} and Apc^{cKO}; Nle^{cKO} small intestinal epithelium. Two bands of similar intensity are amplified from $Apc^{flox/del}$ (top) and $Nle^{flox/del}$ (bottom) DNA (T). The wt allele appears on the gel for *Apc* but not for *Nle*. (C) Weight curve of Control, Apc^{cKO} and Apc^{cKO}; Nle^{cKO} mice following tamoxifen injection. *, $p<0.05$ ***, $p<0.001$ according to Student's t-test. (D) Kaplan-Meier survival curve of Control, Apc^{cKO} and Apc^{cKO}; Nle^{cKO} mice following tamoxifen injection. The difference between Apc^{cKO} and Apc^{cKO}; Nle^{cKO} is significant with $p<0.05$ according to Mann-Whitney Wilcoxon test. (E) Hematoxylin–eosin staining of intestinal epithelium sections from Control, Apc^{cKO} and Apc^{cKO}; Nle^{cKO} small intestines at day 2 pi. Black bars indicate the crypt compartment (enlarged in the Apc^{cKO}). Scale bars, 50 μm.

Figure 2 *Nle* loss-of-function limits the expansion of the proliferative compartment expansion despite Wnt pathway hyperactivation. (A) β-catenin immunostaining (brown) counterstained with hematoxylin (blue) on intestinal epithelium sections from Control, Apc^{cKO} and Apc^{cKO}; Nle^{cKO} intestines at day 2 pi. The second lane shows magnified views of framed regions. Scale bars, 50 μm. (B) RT-qPCR performed on total RNA from Control, Nle^{cKO}, Apc^{cKO} and Apc^{cKO}; Nle^{cKO} intestinal epithelium extracts at day 2 pi. Graphs represent the mean fold changes ± S.E.M. for Wnt transcriptional target genes *c-Myc* and *Axin2*. $n \geq 3$ for each genotype. *, $p<0.05$ **, $p<0.01$ ***, $p<001$ according to Student's t-test. (C) BrdU immunostaining (brown) counterstained with hematoxylin (blue) on intestinal epithelium sections from Control, Apc^{cKO} and Apc^{cKO}; Nle^{cKO} intestines at day 2 pi harvested 2 hours after BrdU injection. Black bars indicate the extension of the proliferative compartment. Scale bars, 50 μm. (D) Histogram showing the mean proportion (± S.E.M.) of BrdU-positive cells in the proliferative compartment in Control, Apc^{cKO} and Apc^{cKO}; Nle^{cKO} small intestines. Twenty-five transverse crypt sections were scored per mouse, n = 4 for each genotype. The means were not significantly different among genotypes according to Mann-Whitney Wilcoxon test.

Figure 3 *Nle* loss-of-function restores cell cycle exit and differentiation in the *Apc*-deficient epithelium. (A) BrdU immunostaining (brown) counterstained with Hematoxylin (blue) on intestinal epithelium sections from Control, Apc^{cKO} and Apc^{cKO}; Nle^{cKO} intestines at day 3 pi harvested 2 hours or 48 hours after BrdU injection. Plain black bars indicate the proliferative compartment. Dotted black bars indicate the range of proliferative cell migration within 48 hours. Scale bars, 50 µm. (B) Cleaved-Caspase 3 immunostaining (brown) counterstained with Hematoxylin (blue) on intestinal epithelium sections from Control, Apc^{cKO} and Apc^{cKO}; Nle^{cKO} intestines at day 2 pi. Arrowheads indicate Caspase 3-positive cells. Scale bars, 50 µm. (C) MUC2 immunostaining (brown) counterstained with Hematoxylin (blue) on intestinal epithelium sections from Control, Apc^{cKO} and Apc^{cKO}; Nle^{cKO} intestines at day 2 pi. Scale bars, 50 µm. (D) Chromogranin A immunostaining (brown) counterstained with Hematoxylin (blue) on intestinal epithelium sections from Control, Apc^{cKO} and Apc^{cKO}; Nle^{cKO} intestines at day 2 pi. Scale bars, 50 µm. (E) Histogram showing the mean number (+/-SEM) of Caspase 3 positive cells per crypt in Control, Apc^{cKO} and Apc^{cKO}; Nle^{cKO} intestines at day 2 pi. 30 transverse crypts were scored per mouse, n≥3 for each genotype. *, $P<0.05$ Mann-Whitney Wilcoxon test. (F) RT-qPCR performed on total RNA from Control, Apc^{cKO} and Apc^{cKO}; Nle^{cKO} intestinal crypt extracts at day 2 pi. Graphs represent the mean fold changes ± S.E.M. for differentiation markers *Mucin 2* (*Muc2*) and *Chromogranin A* (*ChromoA*). n ≥ 3 for each genotype. *, $p<0.05$ **, $p<0.01$ according to Mann-Whitney Wilcoxon test.

Figure 4 *Nle* loss-of-function leads to ribosome biogenesis defects and p53 stabilization in the *Apc*-deficient epithelium. (A) Simplified diagram illustrating the main steps of ribosome biogenesis in eukaryotic cells. Blue arrows represent the primers used to measure the levels of ribosomal RNAs by RT-qPCR. FISH probes used to detect its1 (red) and its2 (green) sequences from precursors of the small and large ribosomal subunits, respectively, are indicated. (B) RT-qPCR performed on total RNA from Control, Apc^{cKO} and Apc^{cKO}; Nle^{cKO} intestinal crypt extracts at day 2 pi. Graphs represent the mean fold changes ± S.E.M. for the different amplicons. n = 4 for each genotype. *, $p<0.05$ **, $p<0.01$ ***, $p<0.001$ according to Student's t-test. (C) FISH for its1 (red) or its2 (yellow) counterstained with Hoechst (blue) on intestinal epithelium sections from Control, Apc^{cKO} and Apc^{cKO}; Nle^{cKO} intestines. Scale bars, 50 µm. (D) p53 immunostaining (brown)

counterstained with Hematoxylin (blue) on intestinal epithelium sections from Control, Apc^{cKO} and Apc^{cKO}; Nle^{cKO} intestines at day 2 pi. Lateral bars indicate the position of the crypt domain for Control and Apc^{cKO}; Nle^{cKO} and of the enlarged crypt-like compartment for Apc^{cKO}. Scale bars, 50 µm.

Figure 5 The double mutant transcriptome is the sum of simple mutant transcriptomes. (A) Principal Component Analysis (PCA) of the samples. PC2 is plotted against PC1. Apc^{cKO} (A) and Apc^{cKO}; Nle^{cKO} (AN) are distinguishable from Control (C) and Nle^{cKO} (N) according to PC1, whereas N and AN are distinguishable from C and A according to PC1, meaning that PC1 corresponds to *Apc* loss-of-function and PC2 corresponds to *Nle* loss-of-function. (B) K-means clustering on all genes normalized by their maximum expression among the samples. (C) List and description of the 8 theoretical categories of genes according to the model-based analysis. -: no change; N: change in all Nle^{cKO} samples including double mutant ones; A: change in all Apc^{cKO} samples including double mutant ones; and D: change in double mutant Apc^{cKO}; Nle^{cKO} different from that predicted by the additive combination of N and A. (D) Histogram showing the distribution of genes among the 8 categories at day 1 pi and day 2 pi. The number of genes assigned to each category is indicated at both timings. (E) Genes in the [A|N|-] and [A|N|D] categories were separated into clusters by the direction of the A, N and D fold changes at day 2 pi. Gene number is plotted on the left of each heatmap. For each cluster, genes relevant to the analyzed phenotypes are indicated, as well as the most significantly enriched gene (black) and phenotype (blue) ontology terms from MouseMine. (F) Histograms showing the expression variation at day 2 pi of some cell cycle inhibitor-coding mRNAs (blue), p53 transcriptional targets (red), Wnt transcriptional targets (purple) and transcripts enriched in ISCs (red). ns, fold change not significant.

Figure 6 *Nle* loss-of-function causes a diminution of mature rRNA levels and global protein synthesis in the *Apc*-deficient epithelium. (A) RT-qPCR for 18S and 28S rRNA performed on total RNA from Control, Apc^{cKO} and Apc^{cKO}; Nle^{cKO} intestinal crypt extracts at day 2 pi. Graphs represent the mean fold changes ± S.E.M. for the different amplicons. n = 4 for each genotype. *, $p<0.05$ **, $p<0.01$ according to Student's t-test. (B) Anti-puromycin immunoblotting of protein extracts for identical number of crypts cells from Control, Apc^{cKO} and Apc^{cKO}; Nle^{cKO} intestines at day 2 pi. (C) Histogram showing the mean

normalized signal intensity ± S.E.M from the immunoblot shown in (B). n = 4 for each genotype. *, p<0.05 according to Mann–Whitney Wilcoxon test.

Figure 7 *Apc* loss-of-function attenuates stem cell loss following *Nle* deletion. (A) RT-qPCR performed on total RNA from Control, Nle^{cKO}, Apc^{cKO} and Apc^{cKO}; Nle^{cKO} intestinal crypt extracts at day 2 pi. Graphs represent the mean fold changes ± S.E.M. for ISC markers Lgr5 and Olfm4. n = 4 for each genotype. *, p<0.05 **, p<0.01 ***, p<001 according to Student's t-test. (B) In situ hybridization for Olfm4 mRNA (brown) counterstained with Hematoxylin (blue) on intestinal epithelium sections from Control, Nle^{cKO}, Apc^{cKO} and Apc^{cKO}; Nle^{cKO} intestines. The second lane shows magnified views of framed regions. Scale bars, 50 µm. (C) p53 immunostaining (brown) counterstained with Hematoxylin (blue) on crypt sections from Apc^{cKO}; Nle^{cKO} intestines at days 2, 3 and 4 pi. Asterisks indicate p53-positive CBCs. Scale bars, 25 µm. (D) BrdU immunostaining (brown) counterstained with Hematoxylin (blue) on crypt sections from Control, Nle^{cKO}, Apc^{cKO} and Apc^{cKO}; Nle^{cKO} intestines at day 2 pi harvested 2 hours after BrdU injection. Asterisks indicate BrdU-positive CBCs. Scale bars, 25 µm.

Figure 8 Apc^{cKO} intestinal organoids show increased tolerance to *Nle*-deficiency and p53 stabilization. (A) Histogram showing the mean percentage (± S.E.M.) of organoid formation and survival at day 4 pi from an initial culture of 400 crypts per well from Control, Nle^{cKO}, Apc^{cKO} and Apc^{cKO}; Nle^{cKO} intestines harvested at day 1 pi. n ≥ 3 experiments for each genotype. (B) Pictures of organoids obtained from Control, Nle^{cKO}, Apc^{cKO} and Apc^{cKO}; Nle^{cKO} crypts. The top lane shows a global view of a well for each genotype at day 4 pi. The middle lane (resp. bottom lane) shows the morphology of organoids of the different genotypes at day 4 (resp. 6) pi. (C) Histogram showing the mean percentage (± S.E.M.) of healthy organoids after 48h culture with various concentration of nutlin-3. (D) Pictures of Control and Apc^{cKO} organoids after 48h in mock and 10µM nutlin-3 culture conditions. Under nutlin-3 treatment, many Control organoids displayed abnormal morphology (star) with absence of budding, swelling and increased opacity likely resulting from increased accumulation of dead cells in the lumen while some Apc^{cKO} spheroids were of irregular shape, opaque and collapsed (arrowhead). Such unhealthy structures were usually degenerating in the following days of culture. *, p<0.05 **, p<0.01 according to Mann-Whitney Wilcoxon test. Scale bars, 150 µm.

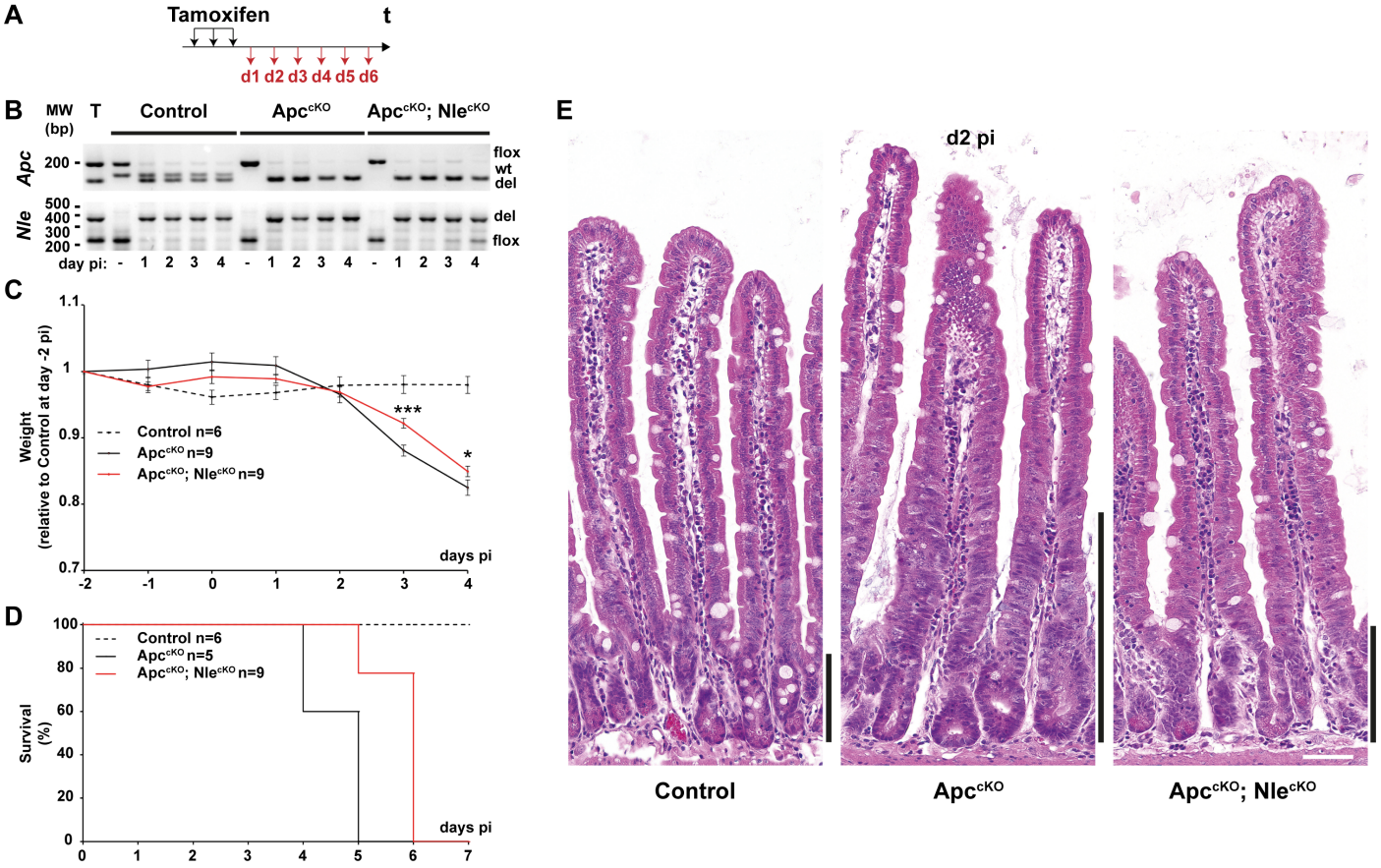
A
Tamoxifen
t
d1 d2 d3 d4 d5 d6
B
MW (bp)
T
Control
Apc^cKO
Apc^cKO; Nle^cKO
Apc
Nle
200
500
400
300
200
flox
wt
del
del
flox
day pi: - 1 2 3 4 - 1 2 3 4 - 1 2 3 4
C
Weight (relative to Control at day -2 pi)
1.1
1
0.9
0.8
0.7
Control n=6
Apc^cKO n=9
Apc^cKO; Nle^cKO n=9
***
*
days pi
-2 -1 0 1 2 3 4
D
Survival (%)
100
80
60
40
20
0
Control n=6
Apc^cKO n=5
Apc^cKO; Nle^cKO n=9
days pi
0 1 2 3 4 5 6 7
E
d2 pi
Control
Apc^cKO
Apc^cKO; Nle^cKO

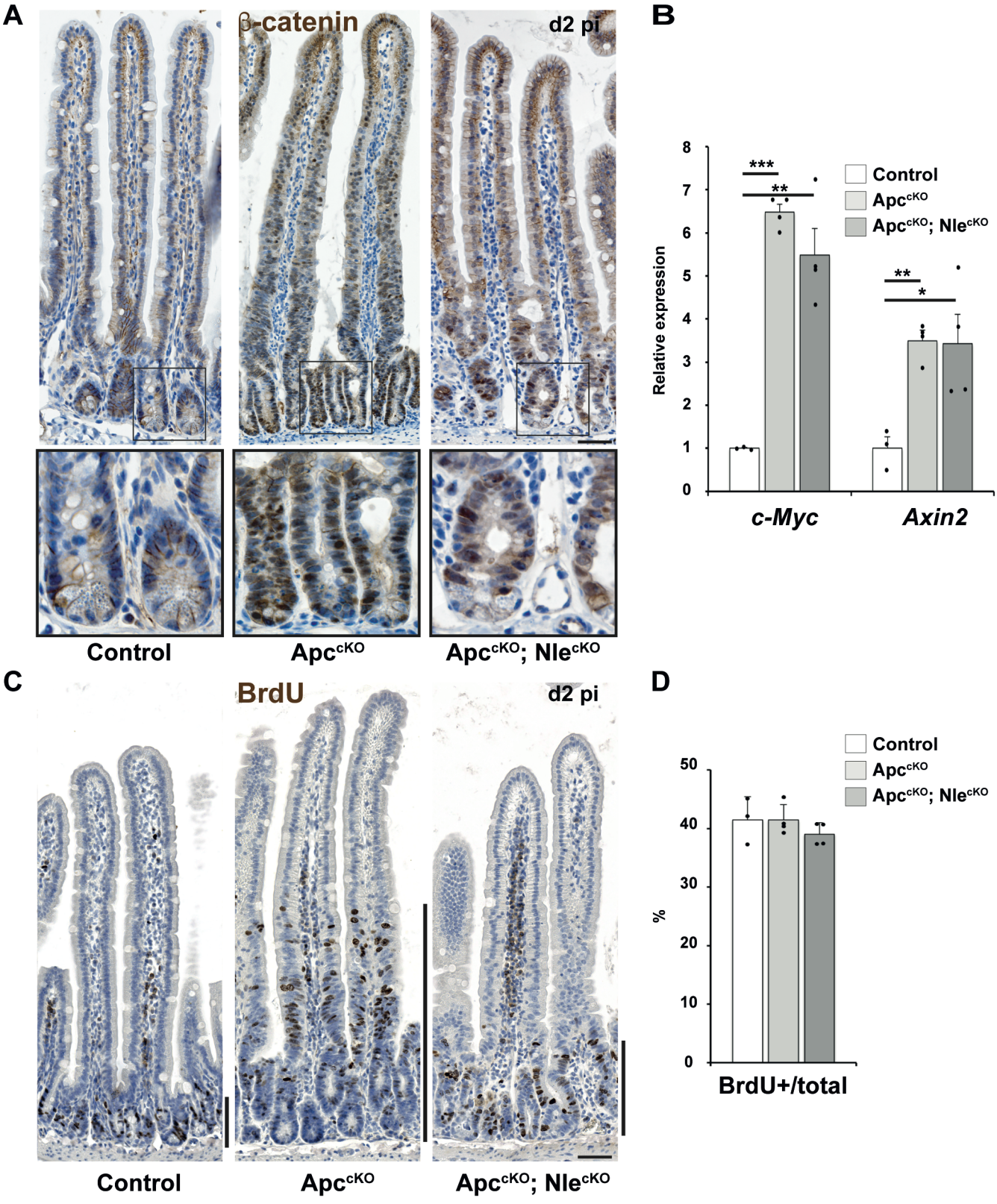
A
β-catenin
d2 pi
Control
Apc^cKO
Apc^cKO; Nle^cKO
B
Relative expression
Control
Apc^cKO
Apc^cKO; Nle^cKO
***
**
**
*
c-Myc
Axin2
C
BrdU
d2 pi
Control
Apc^cKO
Apc^cKO; Nle^cKO
D
%
Control
Apc^cKO
Apc^cKO; Nle^cKO
BrdU+/total

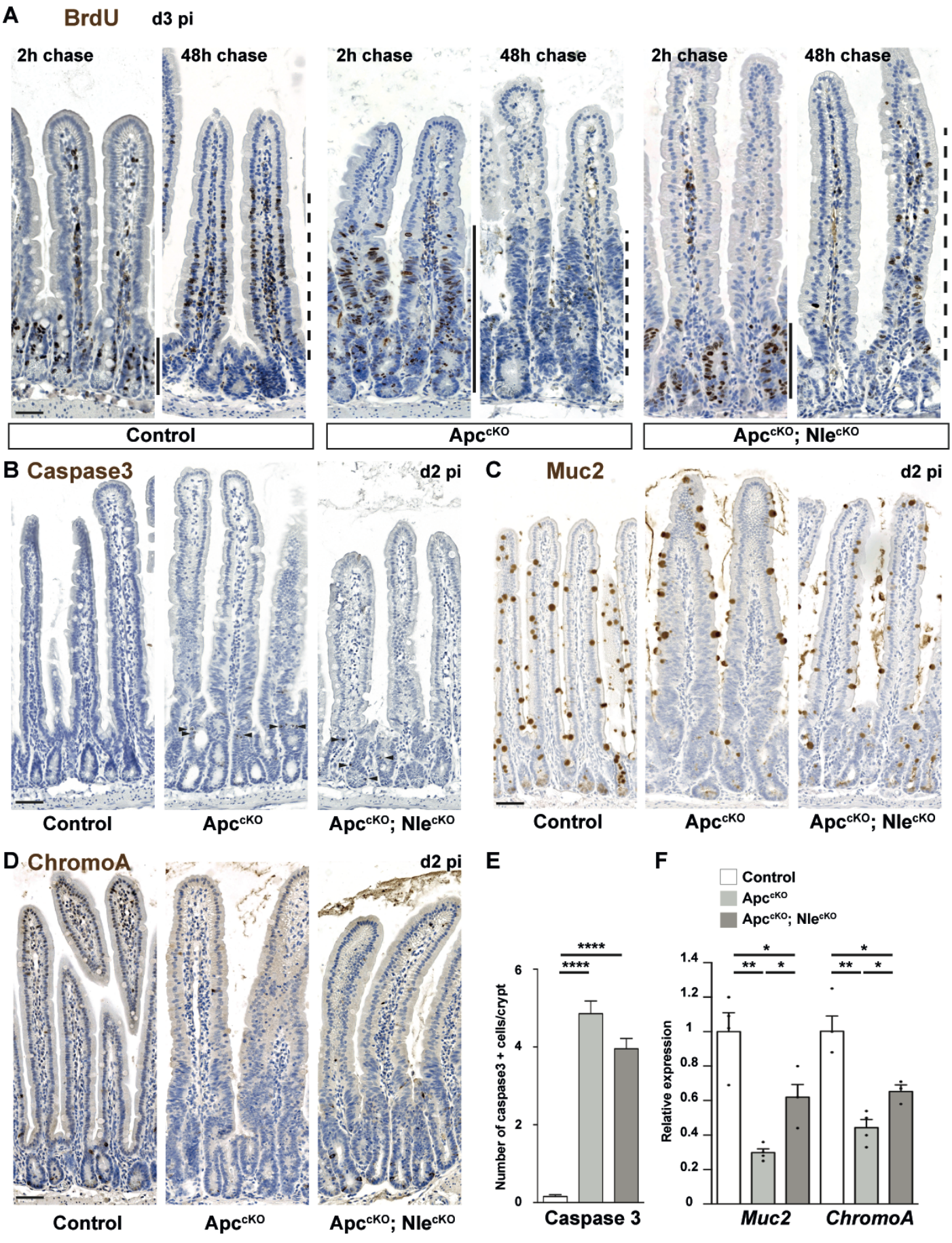
A
BrdU
d3 pi
2h chase
48h chase
2h chase
48h chase
2h chase
48h chase
Control
Apc^cKO
Apc^cKO; Nle^cKO
B Caspase3
d2 pi
C Muc2
d2 pi
Control
Apc^cKO
Apc^cKO; Nle^cKO
Control
Apc^cKO
Apc^cKO; Nle^cKO
D ChromoA
d2 pi
Control
Apc^cKO
Apc^cKO; Nle^cKO
E
Number of caspase3 + cells/crypt
Caspase 3
F
Control
Apc^cKO
Apc^cKO; Nle^cKO
Relative expression
Muc2
ChromoA

Figure 3

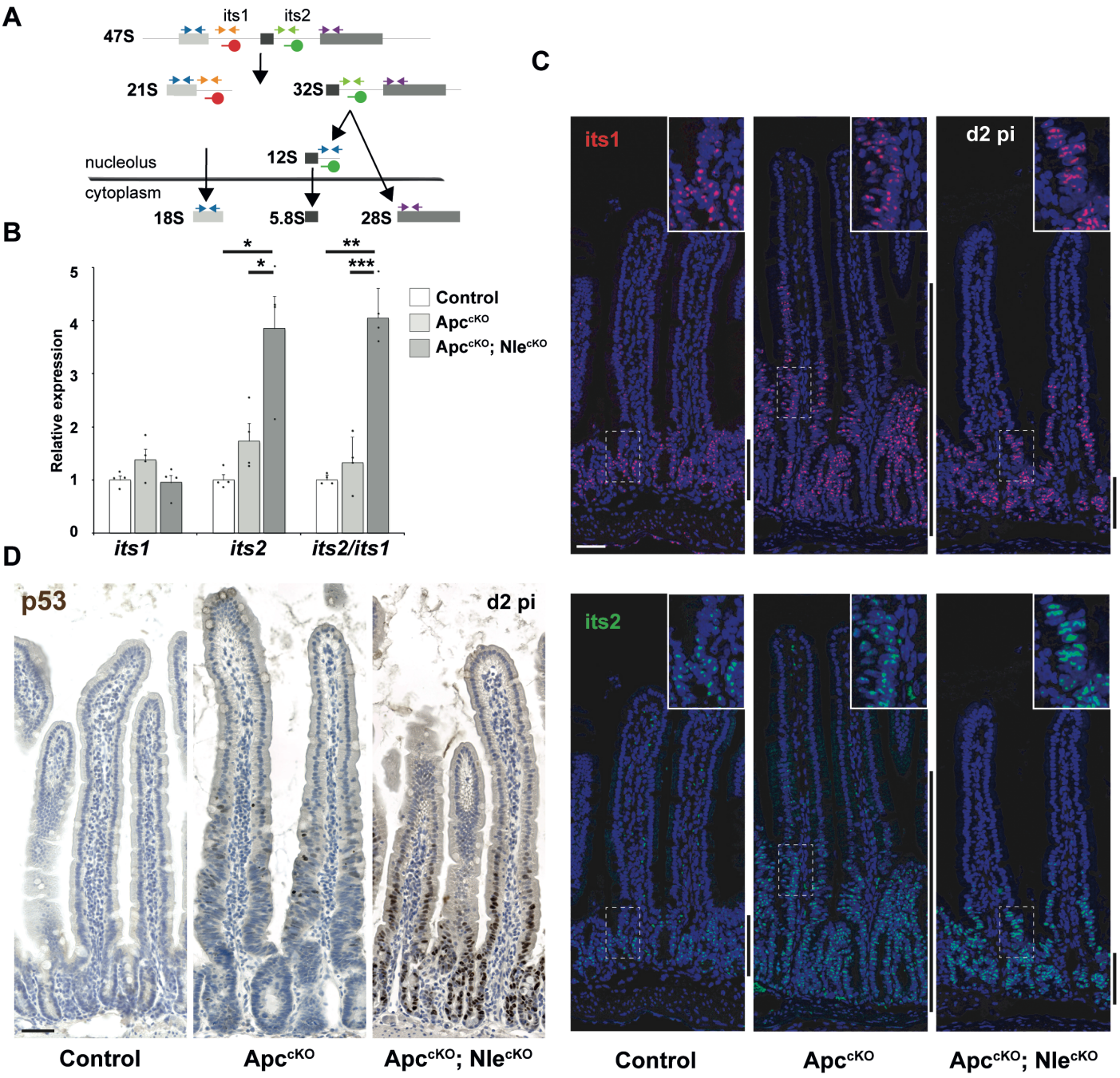
A
its1
its2
47S
21S
32S
12S
nucleolus
cytoplasm
18S
5.8S
28S
B
Relative expression
0
1
2
3
4
5
*
*
**
***
Control
Apc^cKO
Apc^cKO; Nle^cKO
its1
its2
its2/its1
C
its1
d2 pi
its2
Control
Apc^cKO
Apc^cKO; Nle^cKO
D
p53
d2 pi
Control
Apc^cKO
Apc^cKO; Nle^cKO

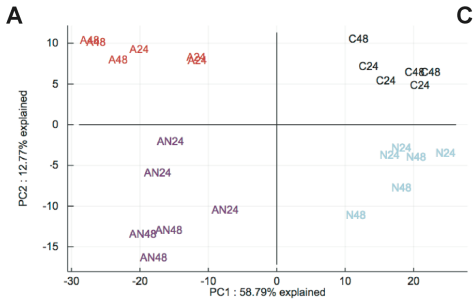

C

Label	Description
[-|-|-]	No variation according to the genotype
[A|-|-]	Gene expression variation due only to Apc loss-of-function in Apc^{cKO} and in Apc^{cKO};Nle^{cKO}
[-|N|-]	Gene expression variation due only to Nle loss-of-function in Nle^{cKO} and in Apc^{cKO};Nle^{cKO}
[A|N|-]	Gene expression variation due to both Nle loss-of-function and Apc loss-of-function. Gene expression in the Apc^{cKO};Nle^{cKO} is the sum of Apc^{cKO} and Nle^{cKO}
[-|-|D]	Gene misregulated only in the Apc^{cKO};Nle^{cKO}
[A|-|D]	Gene misregulated in the Apc^{cKO}, Nle loss-of-function modulates gene expression in the Apc-deficient epithelium but not in the Apc-proficient epithelium
[-|N|D]	Gene misregulated in the Nle^{cKO}, Apc loss-of-function modulates gene expression in the Nle-deficient epithelium but not in the Nle-proficient epithelium
[A|N|D]	Gene expression variation due to both Nle loss-of-function and Apc loss-of-function but gene expression in the Apc^{cKO};Nlke^{cKO} is not the sum of Apc^{cKO} and Nle^{cKO}

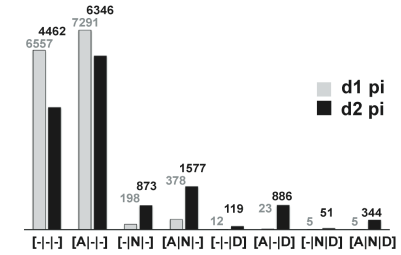

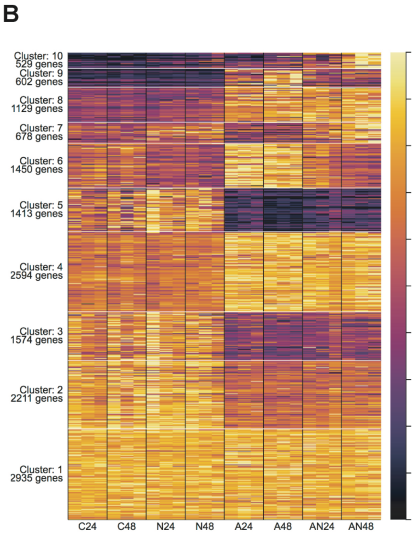

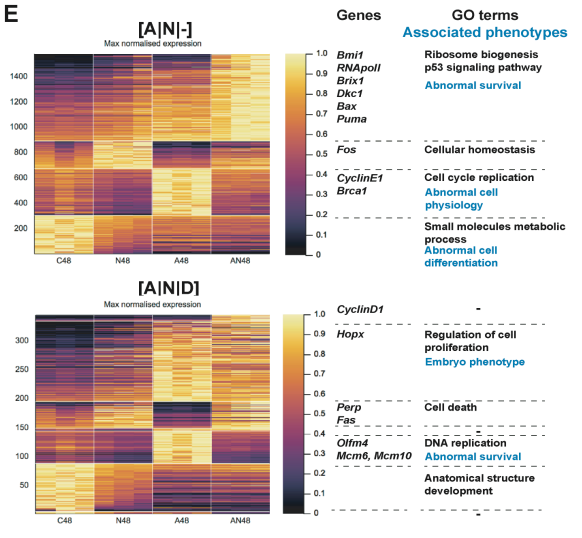

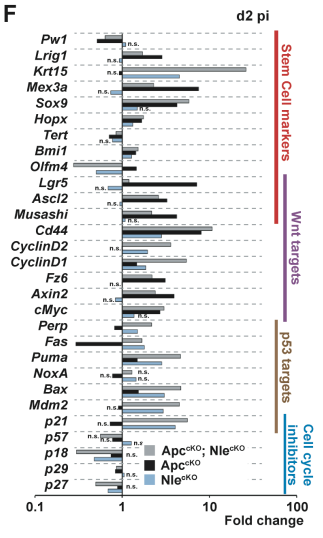

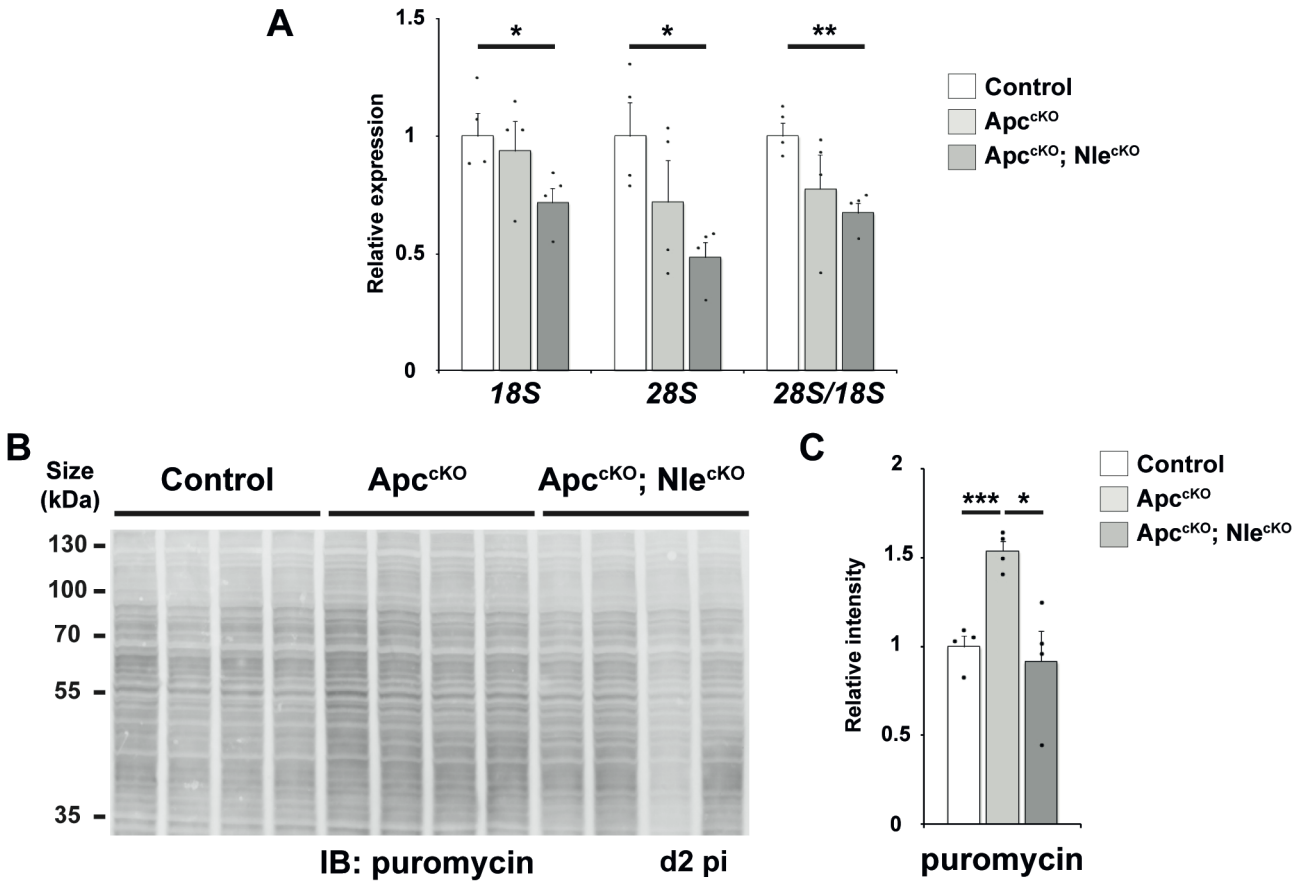
A
1.5
1
0.5
0
Relative expression
*
*
**
18S
28S
28S/18S
Control
Apc^cKO
Apc^cKO; Nle^cKO
B
Size (kDa)
Control
Apc^cKO
Apc^cKO; Nle^cKO
130
100
70
55
35
IB: puromycin
d2 pi
C
2
1.5
1
0.5
0
Relative intensity
***
*
puromycin
Control
Apc^cKO
Apc^cKO; Nle^cKO

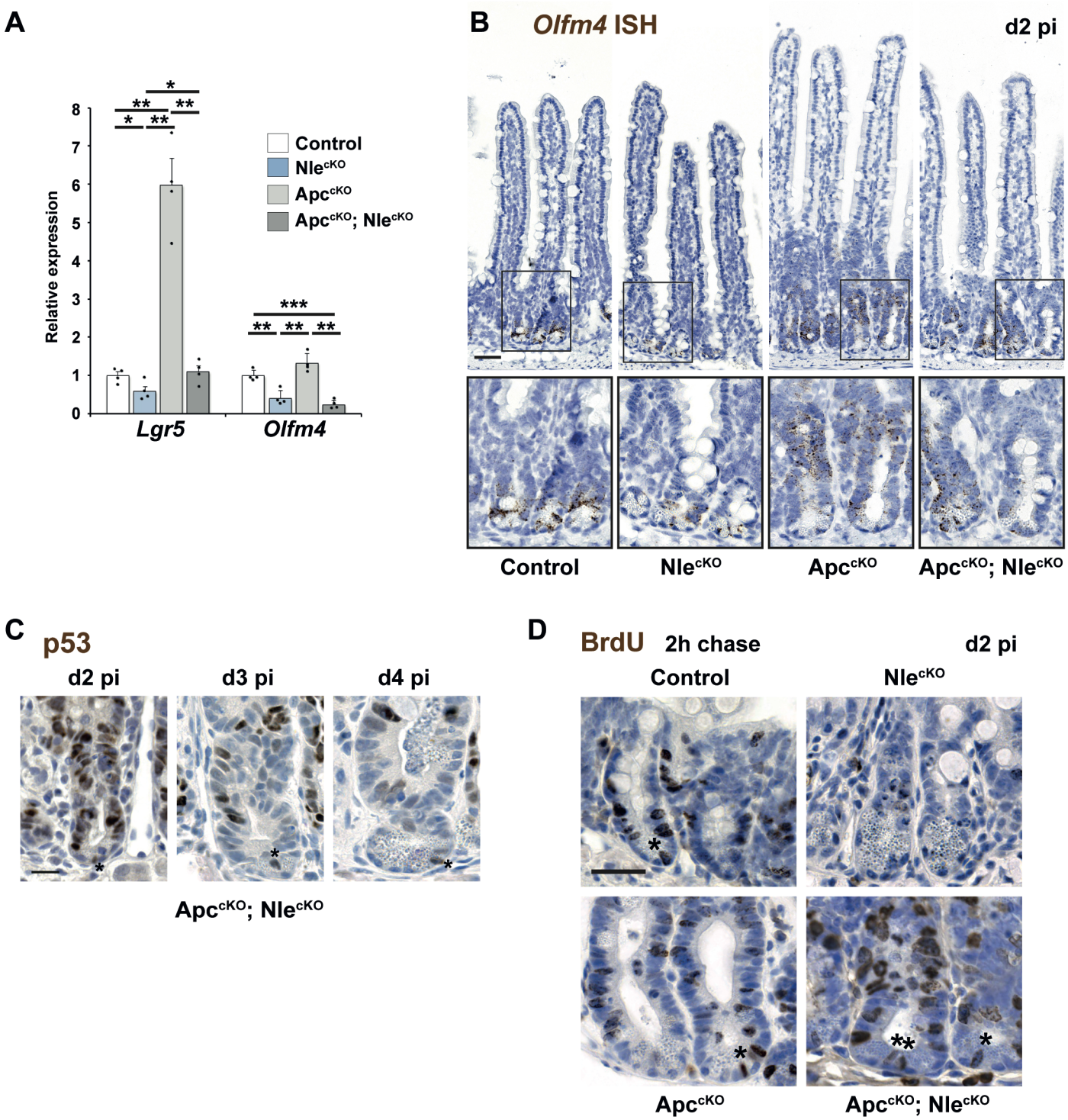
A
Relative expression
Control
Nle^cKO
Apc^cKO
Apc^cKO; Nle^cKO
Lgr5
Olfm4
B
Olfm4 ISH
d2 pi
Control
Nle^cKO
Apc^cKO
Apc^cKO; Nle^cKO
C
p53
d2 pi
d3 pi
d4 pi
Apc^cKO; Nle^cKO
D
BrdU 2h chase
d2 pi
Control
Nle^cKO
Apc^cKO
Apc^cKO; Nle^cKO

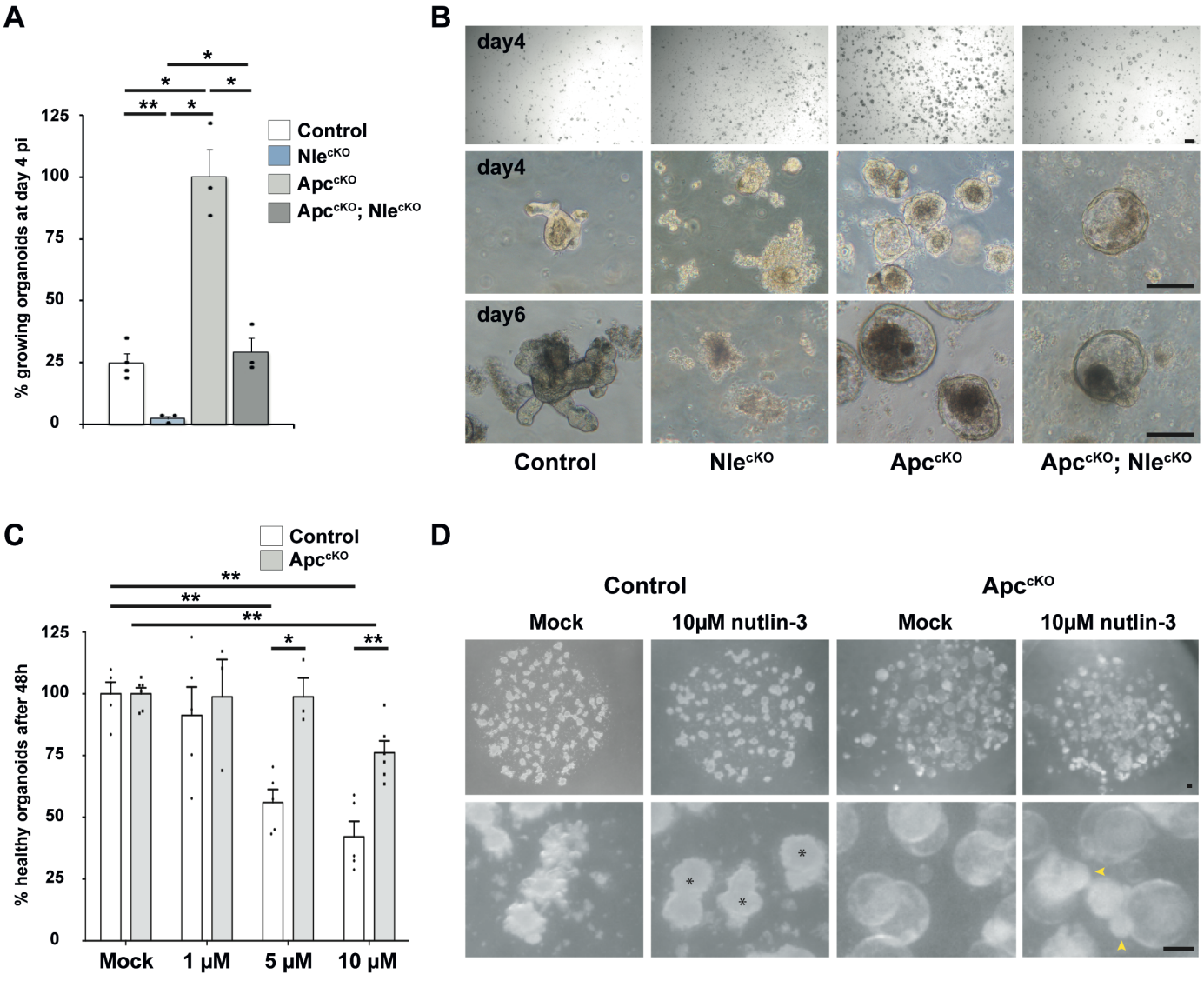
A
% growing organoids at day 4 pi
125
100
75
50
25
0
Control
Nle^cKO
Apc^cKO
Apc^cKO; Nle^cKO
B
day4
day4
day6
Control
Nle^cKO
Apc^cKO
Apc^cKO; Nle^cKO
C
Control
Apc^cKO
% healthy organoids after 48h
125
100
75
50
25
0
Mock
1 μM
5 μM
10 μM
D
Control
Apc^cKO
Mock
10μM nutlin-3
Mock
10μM nutlin-3

Supplementary Figures

Compensation between Wnt-driven tumorigenesis and cellular responses to ribosome biogenesis inhibition in the murine intestinal epithelium

Aurélien Raveux, Aline Stedman, Sabrina Coqueran, Sandrine Vandormael-Pournin, Nick Owens, Béatrice Romagnolo and Michel Cohen-Tannoudji

This file contains 7 supplementary figures and 2 supplementary tables :

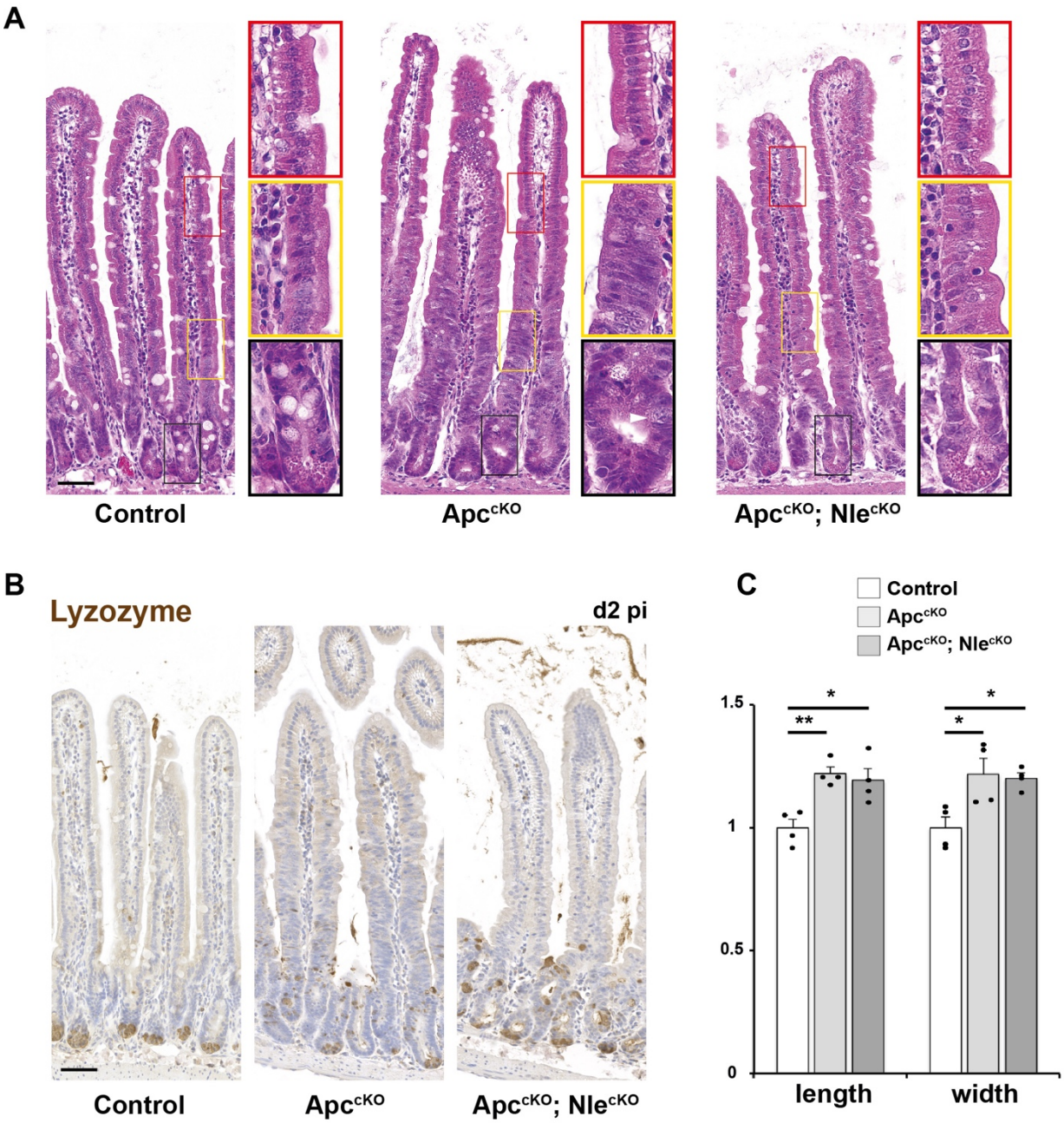

Figure S1 *Nle* loss-of-function only partially restores epithelial histology in the *Apc*-deficient intestine. (A) Hematoxylin–eosin staining of intestinal epithelium sections from Control, Apc^{cKO} and Apc^{cKO}; Nle^{cKO} small intestines at day 2 pi. Scale bars, 50 µm. For each genotype, a portion of the villus is magnified (top) to highlight enterocyte hypertrophia, as well as a portion of the enlarged crypt compartment in the Apc^{cKO} and of the corresponding villus section in the other genotypes (middle) to highlight epithelial architecture restoration in the Apc^{cKO}; Nle^{cKO}, and a magnification of the histological crypt (bottom) is shown to highlight the presence of cells with granules (arrowheads) in the Apc^{cKO} and Apc^{cKO}; Nle^{cKO}. (B) Lysozyme immunostaining (brown) counterstained with Hematoxylin (blue) on intestinal epithelium sections from Control, Apc^{cKO} and Apc^{cKO}; Nle^{cKO} intestines at day 2 pi. Scale bars, 50 µm. (C) Histogram showing the mean (± S.E.M.) length (defined as the lateral membrane section length) and width (defined as the apical or basal membrane section length) of enterocytes in Control, Apc^{cKO} and Apc^{cKO}; Nle^{cKO} villi. Twenty-five transverse sections of enterocytes homogeneously distributed along the jejunum were scored per mouse, n = 4 mice for each genotype. Means were normalized according to mean control measurements. *, $p<0.05$ **, $p<0.01$ according to Student's t-test. Differences that were significant according to Student's t-test were also significant according to Mann-Whitney Wilcoxon test with $p<0.05$.

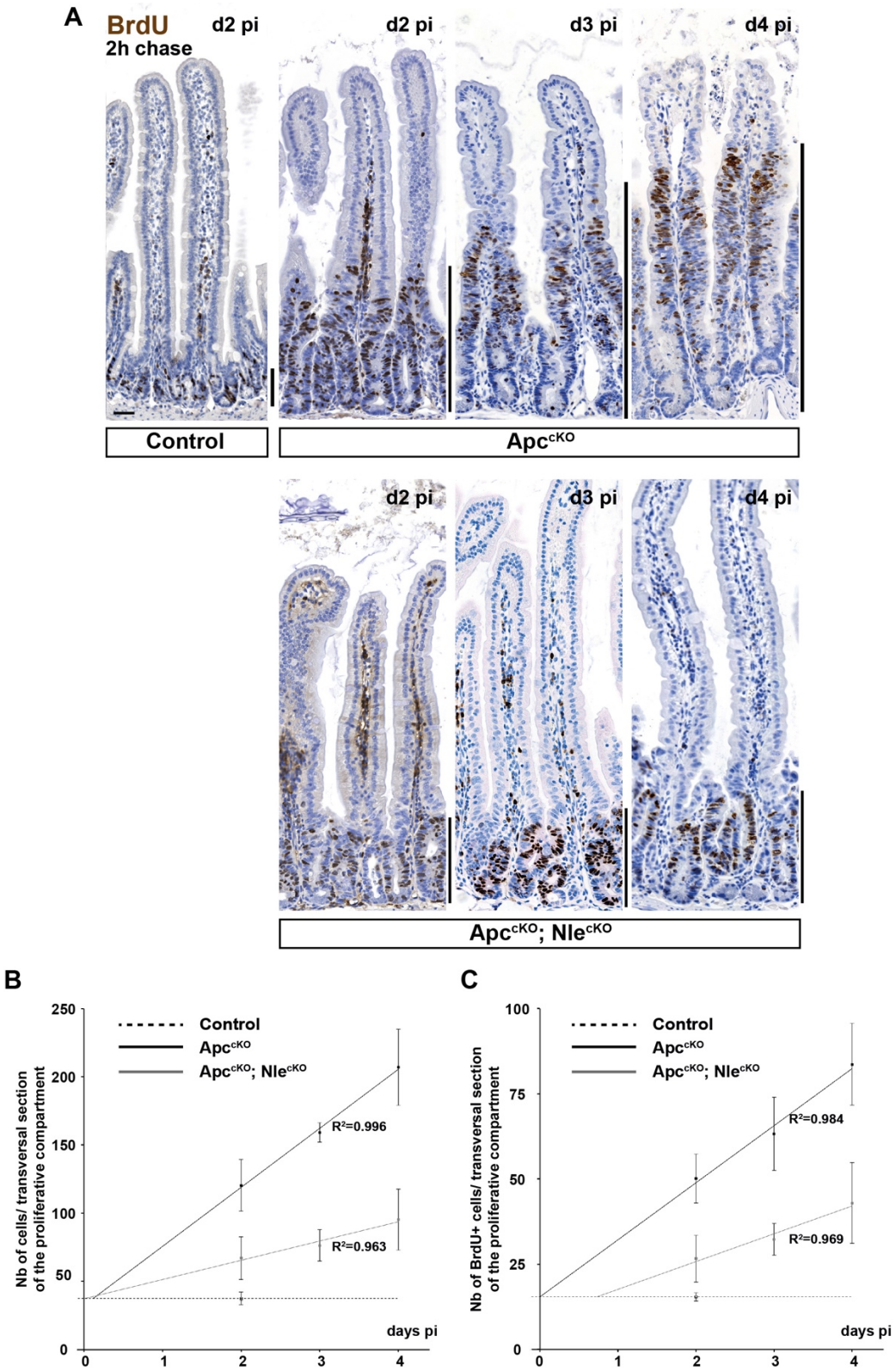

Figure S2 *Nle* loss-of-function reduces proliferative compartment expansion rate in the *Apc*-deficient epithelium. (A) BrdU immunostaining (brown) counterstained with hematoxylin (blue) on intestinal epithelium sections from Control (day 2 pi), Apc^{cKO} and Apc^{cKO}; Nle^{cKO} (days 2, 3 and 4 pi) intestines harvested 2 hours after BrdU injection. Scale bars, 50 µm. (B-C) Graphs showing the mean total cell number (B) and the mean number of BrdU-positive-cells (C) in a transverse section of the proliferative compartment of Control, Apc^{cKO} and Apc^{cKO}; Nle^{cKO} intestines at several timing post tamoxifen injection. Twenty-five transverse crypt sections were scored per mouse, n = 4 for each genotype and each time point. R^2, correlation coefficient with a linear model (plain regression lines). The dotted horizontal line shows baseline Control levels according to day 2 pi measurements. Hypothesizing linear growth, proliferative compartment expansion begins at 0 day pi in the Apc^{cKO} as previously reported [10] and in the Apc^{cKO}; Nle^{cKO}.

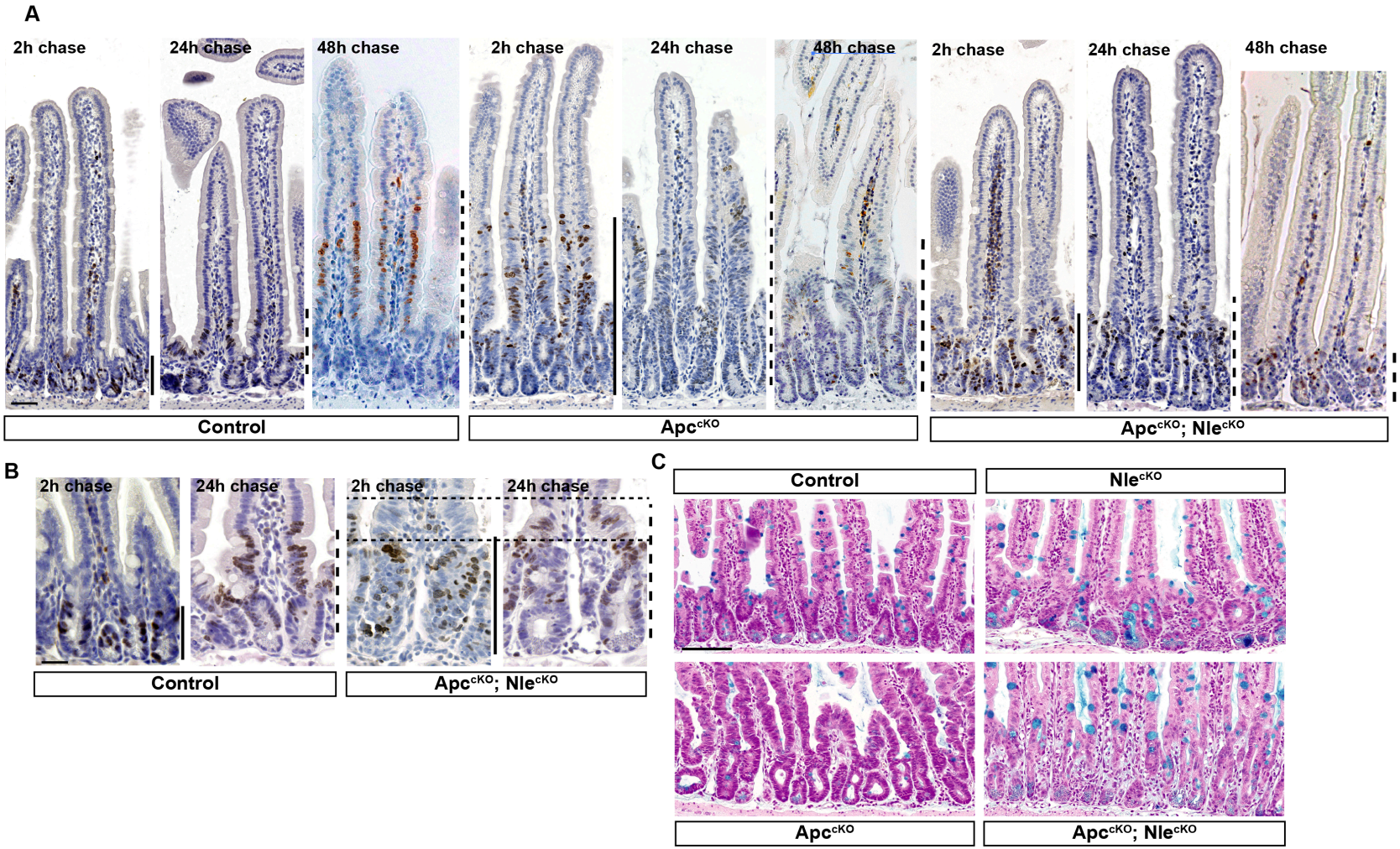

Figure S3 Cell cycle exit is delayed in the double mutant compared to the control. (A) BrdU immunostaining (brown) counterstained with Hematoxylin (blue) on intestinal epithelium sections from Control and Apc^{cKO}; Nle^{cKO} intestines at day 2 pi harvested 2, 24 or 48 hours after BrdU injection. Plain black bars indicate the proliferative compartment. Dotted black bars indicate the range of proliferative cell migration within 24 or 48 hours. Scale bars, 50 µm. (B) BrdU immunostaining (brown) counterstained with Hematoxylin (blue) on crypt sections from Control and Apc^{cKO}; Nle^{cKO} intestines at day 2 pi harvested 2 hours or 24 hours after BrdU injection. Plain black bars indicate the proliferative compartment. The dotted horizontal lines indicate the limits of the double-mutant specific compartment (see text). Scale bars, 25 µm. (C) Alcian blue coloration counterstained with Nuclear Fast Red on intestinal epithelium sections from Control, Nle^{cKO}, Apc^{cKO} and Apc^{cKO}; Nle^{cKO} intestines at day 3 pi. Scale bars, 100 µm.

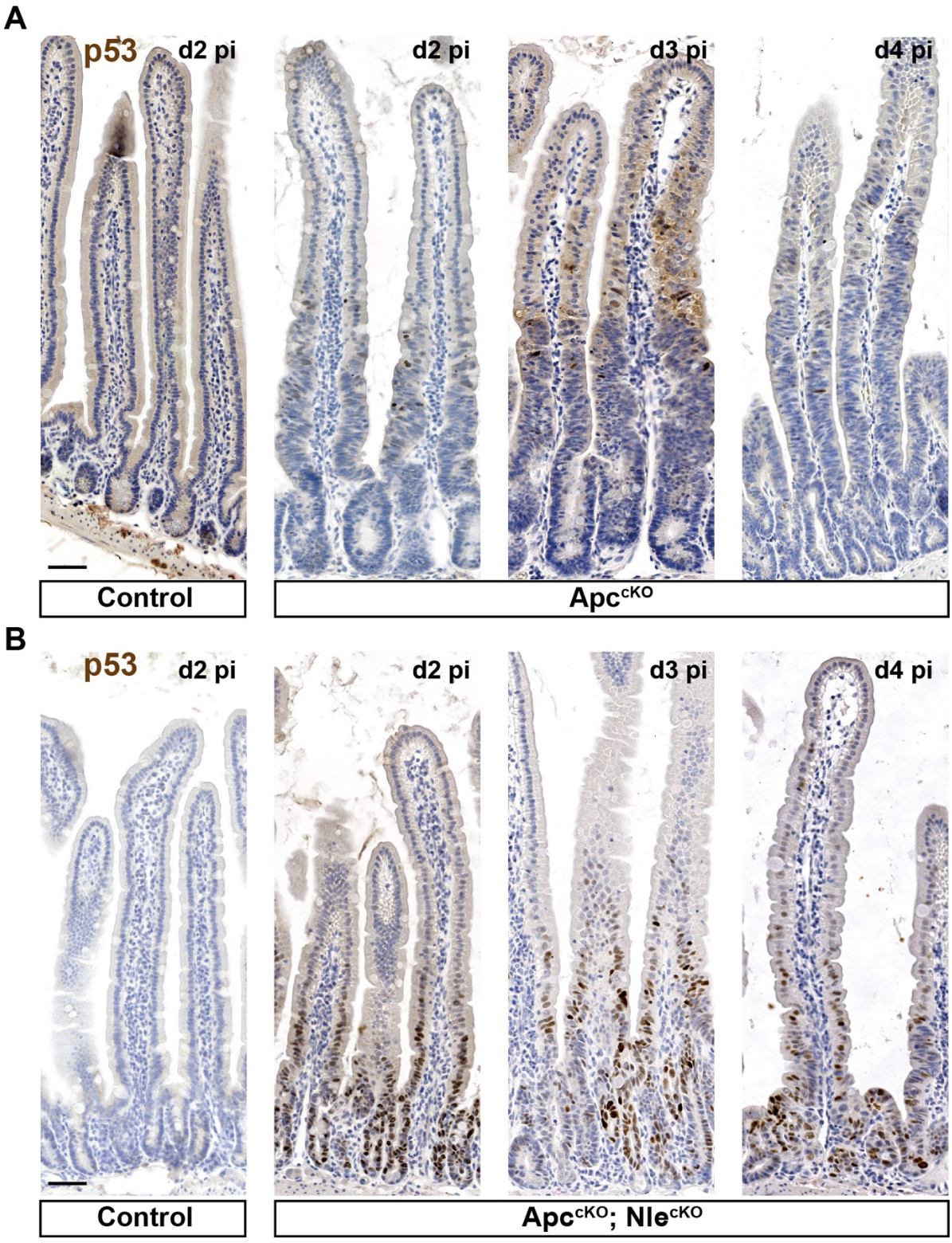

Figure S4 *Nle* loss-of-function induces persistent p53 stabilization in the *Apc*-deficient epithelium. (A) p53 immunostaining (brown) counterstained with Hematoxylin (blue) on intestinal epithelium sections from Control (day 2 pi) and Apc^{cKO} (days 2, 3 and 4 pi) intestines. Scale bars, 50 µm. (B) p53 immunostaining (brown) counterstained with Hematoxylin (blue) on intestinal epithelium sections from Control (day 2 pi) and Apc^{cKO}; Nle^{cKO} (days 2, 3 and 4 pi) intestines. Scale bars, 50 µm.

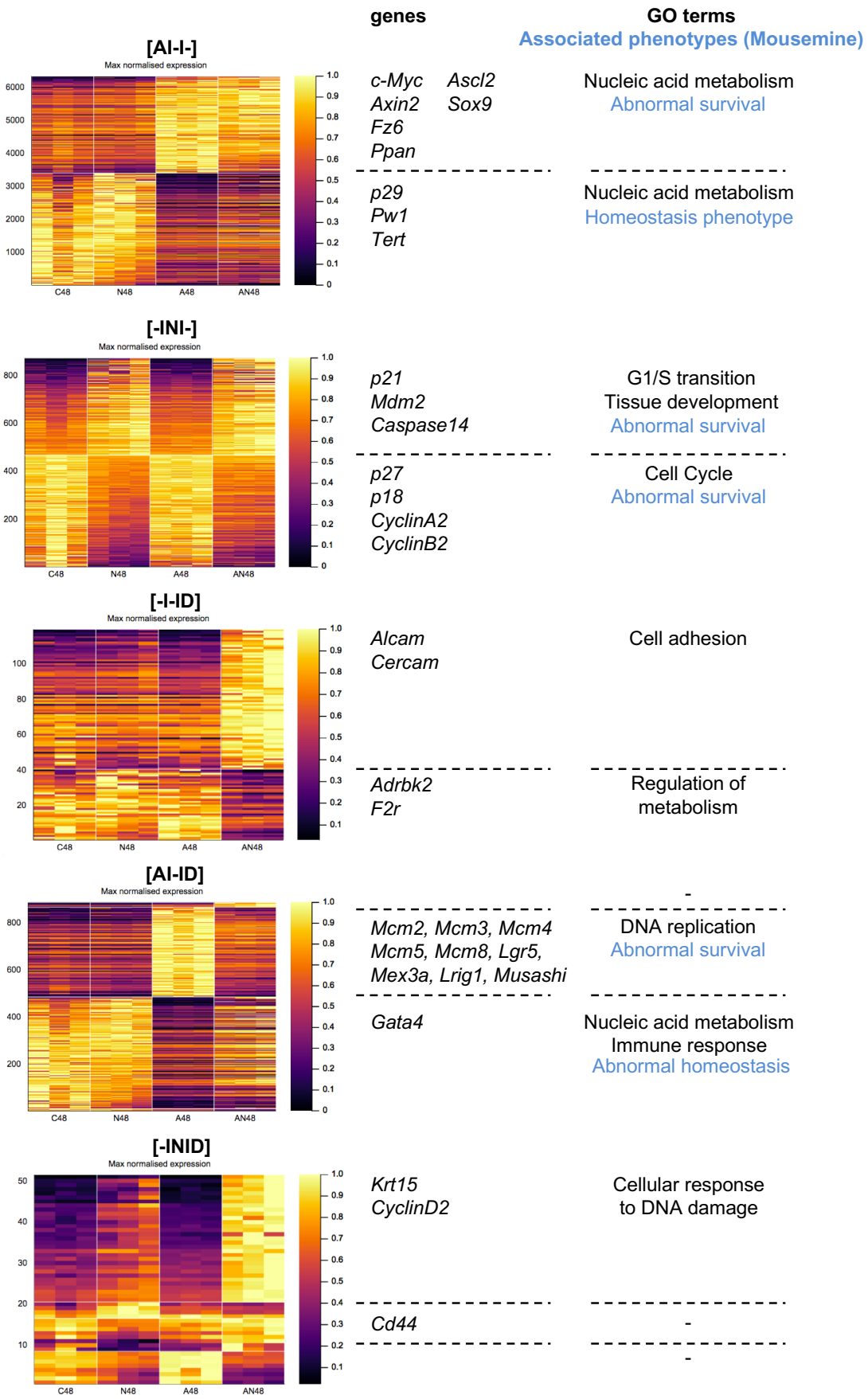

Figure S5 Functional analysis of gene clusters does not indicate signaling pathway interference between *Apc* loss-of-function and *Nle* loss-of-function. Genes in the [A|N|-] and [A|N|D] categories were separated into clusters by the direction of the A, N and D fold changes at day 2 pi. Gene number is plotted on the left of each heatmap. For each cluster, genes relevant to the analyzed phenotypes are indicated, as well as the most significantly enriched gene (black) and phenotype (blue) ontology terms from MouseMine.

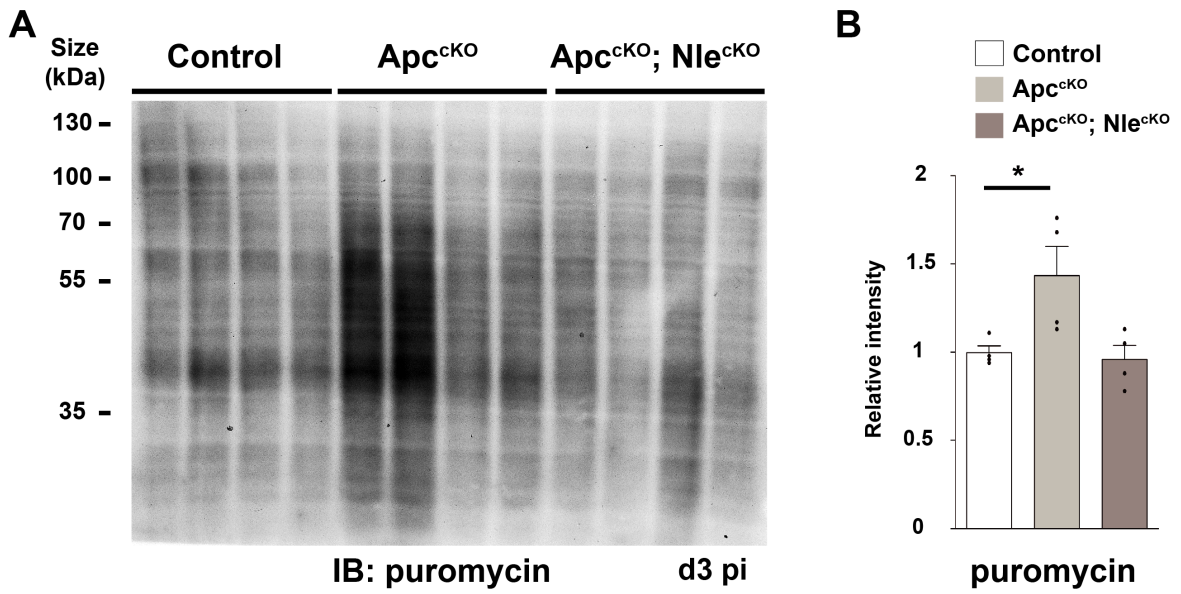

Figure S6 Global protein synthesis at day 3 pi. (A) Anti-puromycin immunoblotting of protein extracts for identical number of crypts cells from Control, Apc^{cKO} and Apc^{cKO}; Nle^{cKO} intestines at day 3 pi. (B) Histogram showing the mean normalized signal intensity ± S.E.M from the immunoblot shown in (A). n = 4 for each genotype. *, $p<0.05$ according to Mann–Whitney Wilcoxon test.

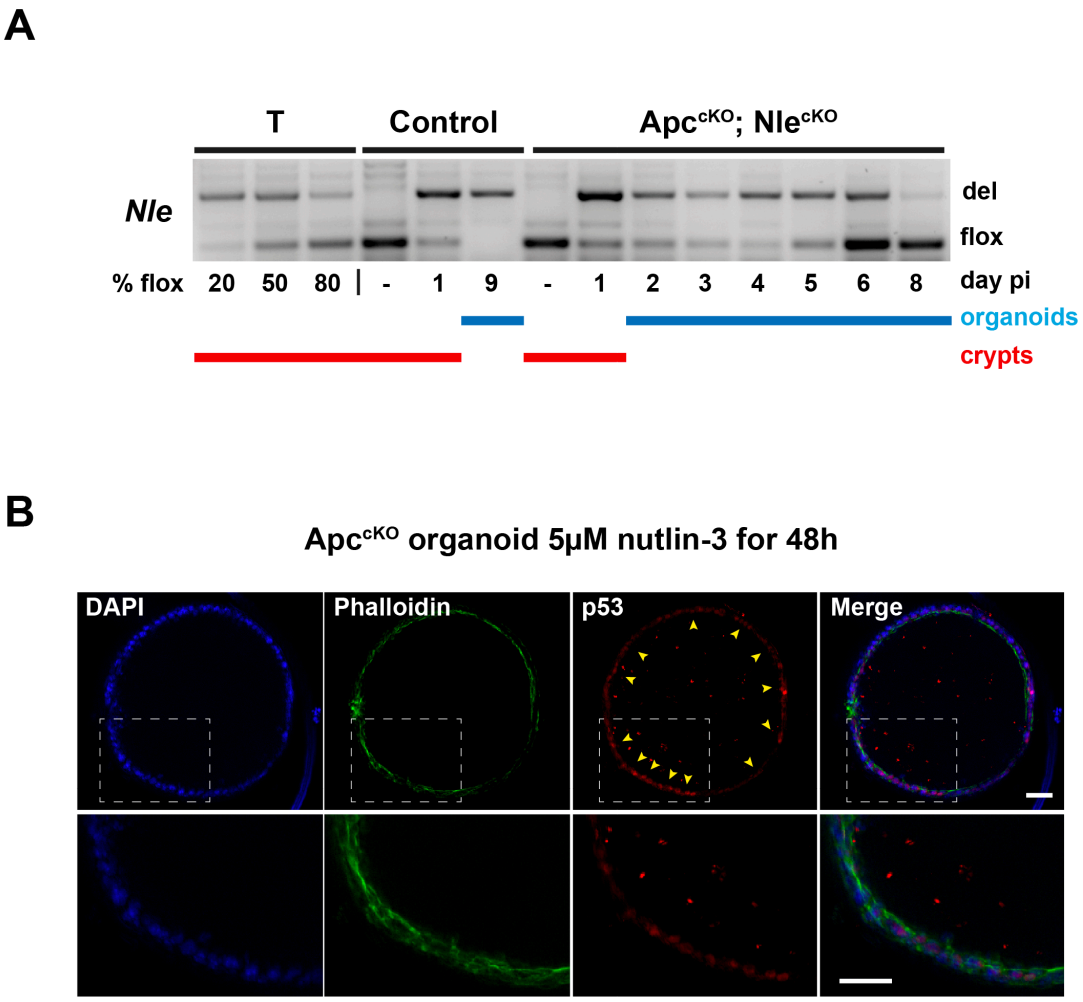

Figure S7 Derivation and nutlin-3 treatment of intestinal organoids (A) Detection of the nonrecombined (flox) and the recombined (del) *Nle* alleles by PCR performed on DNA extracts from Control and Apc;NleVilcKO wells at different time points. Control DNAs with 20%, 50% and 80% flox alleles obtained by mixing $Nle^{flox/+}$ and $Nle^{flox/del}$ DNAs are presented. The Nle^{+} and Nle^{null} alleles are not shown on the gel. (A) p53 immunostaining of an APC^{cKO} organoid cultured for 48h with 5µM nutlin-3. A single optical section is shown. Note the presence of numerous p53 positive nuclei on the whole circumference of the spheroid. Bright dots correspond to non specific staining of debris present in the lumen of the organoid. Bar: 50µM.

Supplementary Table 1: list of primary and secondary antibodies

Antibodies	Reference	Dilution used
anti-cleaved Caspase 3	9661L Ozyme	1/200
anti-BrdU	347580 BD	1/150
anti-β-catenin	C19220 BD	1/50
anti-p53	CM5-p Leica	1/500
anti-lysozyme	A0099 Dako	1/1000
anti-Muc2	sc-15334 Santa-Cruz	1/200
anti-ChromoA	sc-1488 Santa-Cruz	1/300
anti-puromycin	5B12, David *et al*., JCB 2012	1/5000
Biotinylated goat anti-rabbit IgG	E0432 Dako	1/400
Biotinylated goat anti-mouse IgG	E0433 Dako	1/400

Supplementary Table 2: Sequences of RT-qPCR primers

Target gene	Forward primer	Reverse primer
Olfm4	ATCAGCGCTCCTTCTGTGAT	AGGGTTCTCTCTGGATGCTG
Lgr5	ACATTCCCAAGGGAGCGTTC	ATGTGGTTGGCATCTAGGCG
Muc2	CAAGGGCTCGGAACTCCAG	CCAGGGAATCGGTAGACATCG
ChromoA	AGTCATCTCCGACTCGCTGT	GGTGTCGCAGGATAGAGAGG
c-Myc	AAGGCCCCCAAGGTAGTG	TGCTCGTCTGCTTGAATGGA
Axin 2	GATTCCCCTTTGACCAGGTGG	CCATTACAAGCAAACCAGAAGT
Its1	TCTGACCTCGCCACCCTA	CCTCGTAGACACGGAAGAGC
Its2	TGTGTGTGTTTGGGTCTTGC	GGATACCACCTCTCTCCGTTC
28S	TCATCAGACCCCAGAAAAGG	GATTCGGCAGGTGAGTTGTT
18S	CGGCTACCACATCCAAGGAA	GCTGGAATTACCGCGGCT